Article

Rewiring of cortical glucose metabolism fuels human brain cancer growth

https://doi.org/10.1038/s41586-025-09460-7

Received: 30 November 2023

Accepted: 28 July 2025

Published online: 3 September 2025

Open access

Check for updates

Andrew J. Scott[1,2,21], Anjali Mittal[3,4,5,21], Baharan Meghdadi[3,4,5,21], Alexandra O'Brien[1], Justine Bailleul[6,7], Palavalasa Sravya[1], Abhinav Achreja[2,3,4,8], Weihua Zhou[1,2], Jie Xu[1], Angelica Lin[1], Kari Wilder-Romans[1], Ningning Liang[1], Ayesha U. Kothari[1], Navyateja Korimerla[1], Donna M. Edwards[1], Zhe Wu[9], Jiane Feng[9], Sophia Su[1], Li Zhang[9], Peter Sajjakulnukit[9], Anthony C. Andren[9], Junyoung O. Park[10], Johanna ten Hoeve[11], Vijay Tarnal[12,13], Kimberly A. Redic[14], Nathan R. Qi[9], Joshua L. Fischer[15], Ethan Yang[15], Michael S. Regan[16], Sylwia A. Stopka[16], Gerard Baquer[16], Krithika Suresh[1,17], Jann N. Sarkaria[18], Theodore S. Lawrence[1,2], Sriram Venneti[19], Nathalie Y. R. Agar[16], Erina Vlashi[6,7], Costas A. Lyssiotis[2,9,20,22] ✉, Wajd N. Al-Holou[2,13,22] ✉, Deepak Nagrath[2,3,4,5,22] ✉ & Daniel R. Wahl[1,2,13,22] ✉

The brain avidly consumes glucose to fuel neurophysiology[1]. Cancers of the brain, such as glioblastoma, relinquish physiological integrity and gain the ability to proliferate and invade healthy tissue[2]. How brain cancers rewire glucose use to drive aggressive growth remains unclear. Here we infused ^{13}C-labelled glucose into patients and mice with brain cancer, coupled with quantitative metabolic flux analysis, to map the fates of glucose-derived carbon in tumour versus cortex. Through direct and comprehensive measurements of carbon and nitrogen labelling in both cortex and glioma tissues, we identify profound metabolic transformations. In the human cortex, glucose carbons fuel essential physiological processes, including tricarboxylic acid cycle oxidation and neurotransmitter synthesis. Conversely, gliomas downregulate these processes and scavenge alternative carbon sources such as amino acids from the environment, repurposing glucose-derived carbons to generate molecules needed for proliferation and invasion. Targeting this metabolic rewiring in mice through dietary amino acid modulation selectively alters glioblastoma metabolism, slows tumour growth and augments the efficacy of standard-of-care treatments. These findings illuminate how aggressive brain tumours exploit glucose to suppress normal physiological activity in favour of malignant expansion and offer potential therapeutic strategies to enhance treatment outcomes.

Gliomas are the most prevalent malignant brain tumours, originating from glial transformation into aggressive, brain-invading cells[3]. Glioblastoma (GBM), the most common and aggressive primary malignant brain tumour in adults, is marked by its invasiveness, treatment resistance and fatal prognosis[3,4]. Despite standard-of-care treatments including surgical resection, radiation therapy (RT) and temozolomide (TMZ) chemotherapy, GBMs invariably recur, and most patients die within 1–2 years of diagnosis[4]. Poor outcomes are due largely to treatment resistance, with extensive tumour heterogeneity limiting therapeutic efficacy[3,5], but might be overcome by defining and targeting common GBM metabolic vulnerabilities that promote resistance[6–9].

Understanding metabolic activity in tumours is critical to appropriately guide metabolically directed therapy. While approaches such as positron emission tomography (PET) with glucose analogues[10], magnetic resonance spectroscopy and metabolomics can measure glucose uptake and metabolite abundance, stable isotope tracing directly monitors metabolic activity. To determine how nutrients are differentially metabolized, substrates containing heavy (but non-radioactive) isotopes are followed into downstream metabolites, revealing which

[1]Department of Radiation Oncology, University of Michigan, Ann Arbor, MI, USA. [2]Rogel Cancer Center, University of Michigan, Ann Arbor, MI, USA. [3]Laboratory for Systems Biology of Human Diseases, University of Michigan, Ann Arbor, MI, USA. [4]Biointerfaces Institute, University of Michigan, Ann Arbor, MI, USA. [5]Department of Chemical Engineering, University of Michigan, Ann Arbor, MI, USA. [6]Department of Radiation Oncology, David Geffen School of Medicine, University of California, Los Angeles, CA, USA. [7]Jonsson Comprehensive Cancer Center, University of California, Los Angeles, CA, USA. [8]Department of Biomedical Engineering, University of Michigan, Ann Arbor, MI, USA. [9]Department of Molecular and Integrative Physiology, University of Michigan, Ann Arbor, MI, USA. [10]Department of Chemical and Biomolecular Engineering, University of California, Los Angeles, CA, USA. [11]Department of Molecular and Medical Pharmacology, David Geffen School of Medicine, University of California, Los Angeles, CA, USA. [12]Department of Anesthesiology, University of Michigan, Ann Arbor, MI, USA. [13]Department of Neurosurgery, University of Michigan, Ann Arbor, MI, USA. [14]Department of Pharmacy Services, Michigan Medicine, University of Michigan, Ann Arbor, MI, USA. [15]Bruker Daltonics, Billerica, MA, USA. [16]Department of Neurosurgery, Brigham and Women's Hospital, Harvard Medical School, Boston, MA, USA. [17]Department of Biostatistics, University of Michigan, Ann Arbor, MI, USA. [18]Department of Radiation Oncology, Mayo Clinic, Rochester, MN, USA. [19]Department of Pathology, University of Michigan, Ann Arbor, MI, USA. [20]Department of Internal Medicine, Division of Gastroenterology, University of Michigan, Ann Arbor, MI, USA. [21]These authors contributed equally: Andrew J. Scott, Anjali Mittal, Baharan Meghdadi. [22]These authors jointly supervised this work: Costas A. Lyssiotis, Wajd N. Al-Holou, Deepak Nagrath, Daniel R. Wahl. ✉e-mail: clyssiot@umich.edu; wna@med.umich.edu; dnagrath@umich.edu; dwahl@med.umich.edu

pathways are active under different conditions. Applying this methodology to human cancers has revealed suppressed glucose oxidation in kidney cancer[11] and enhanced lactate use, glycolysis and glucose oxidation in lung cancer[12]. Limited applications of this technology to human brain cancer have shown that the tricarboxylic acid (TCA) cycle is active and can be fuelled by both glucose and acetate[13,14]. How active other pathways are in glioma, how this activity differs from adjacent brain tissue and its therapeutic tractability are unanswered questions.

To answer these questions, we infused isotope-labelled nutrients into patients with high-grade gliomas and mice bearing orthotopic GBMs, following their metabolism into downstream pathways in both cancerous and cortical brain tissue. We paired these measurements with metabolic flux models to quantify the absolute rates of in vivo metabolic reactions. We find that aggressive brain cancers shift glucose carbon use away from physiological processes, including TCA cycle oxidation and amino acid neurotransmitter synthesis, in part by salvaging nutrients like serine from the environment. Instead, they preferentially use glucose carbons to synthesize the nucleotides needed to grow. We also find that this metabolic regulation is plastic, with GBMs adaptively upregulating these pathways in response to therapy. Restricting alternative carbon sources by modulating diet shifts GBM metabolism away from biomass production and increases chemoradiation efficacy. Together, these studies present comprehensive measurements comparing metabolic activity in brain tumours to adjacent cortical tissue, revealing tumour-specific metabolic rewiring that can be selectively targeted with precision dietary interventions.

Glucose tracing in intracranial tissue

To identify common metabolic phenotypes across the heterogeneous GBM landscape, we infused uniformly labelled ^{13}C-glucose ([U^{13}C]glucose) into patients with likely GBM undergoing surgical resection and several intracranial patient-derived GBM models. We then determined the downstream metabolic fates of glucose-derived ^{13}C in the cortex and discrete tumour regions using mass spectrometry (MS; Fig. 1a).

Our current surgical practice for patients with glioma with tumours in non-eloquent locations is to perform a supramaximal resection removing the contrast-enhancing tumour, the non-enhancing fluid-attenuated inversion recovery (FLAIR) hyperintense tumour and some of the surrounding cortex[15] (Fig. 1b). In GBM, contrast enhancement occurs when the blood–brain barrier is compromised, typically signifying aggressive, vascular tumour areas. Conversely, FLAIR hyperintense, non-enhancing regions are often infiltrative areas with a less-compromised blood–brain barrier. To acquire a comprehensive understanding of tumour metabolic activity, we investigated how both tumour regions differ from cortical tissue. Eight patients enrolled in this study (Extended Data Table 1). Six of these patients were found to have GBMs, one was diagnosed with *IDH*-mutant anaplastic oligodendroglioma and one was diagnosed with histone H3 G34R mutant grade 4 glioma. In animal studies, three patient-derived orthotopic models with heterogeneous genomic backgrounds were selected based on transcriptional profiling of tumours from our patient cohort, suggesting mesenchymal, proneural and classical features (Extended Data Fig. 1a–c and Supplementary Tables 1 and 2). These features are exhibited respectively by HF2303, GBM38 and GBM12 models[16–19]—although these subtypes may be plastic.

Haematoxylin and eosin (H&E) staining confirmed adequate separation of human samples, with around 80% tumour in enhancing samples, 80% cortex in cortex samples and mixed content in non-enhancing samples (Extended Data Fig. 2a,b). Consistent with adequate separation and magnetic resonance spectroscopy reports[20], human cortex had 2–50-fold higher *N*-acetylaspartate levels than enhancing tumour (Extended Data Fig. 2c). Furthermore, the patient with *IDH*-mutant oligodendroglioma had higher tumour 2HG levels (20–30-fold) than cortex and other patients (Extended Data Fig. 2d). Consistent with previous studies[21], numerous other metabolites differed in absolute levels between cortex and tumour (Extended Data Fig. 2e–i).

In patients, [U^{13}C]glucose infusions lasted for the duration of craniotomy, typically around 3 h. Circulating arterial [U^{13}C]glucose levels (m+6, all 6 carbons labelled) ranged between 20 and 40% of total arterial glucose during surgery and were typically at steady state after 30 min (Fig. 1c). ^{13}C-labelling of arterial lactate (formed by tissue-mediated [U^{13}C]glucose conversion and secretion into circulation) varied among patients and was typically between 10 and 30% (Extended Data Fig. 3a). In mice, [U^{13}C]glucose reached arterial steady state within 30 min with label enrichments of around 50% (Fig. 1d), while circulating lactate labelling reached about 30% (Extended Data Fig. 3b).

After tissue entry, glucose is metabolized through glycolysis (Extended Data Fig. 3c). Liquid chromatography coupled with MS (LC–MS) analysis of tissues from ^{13}C-infused humans and mice revealed similar ^{13}C labelling of upper glycolysis intermediates in GBM and cortex (Fig. 1e,f), suggesting that [U^{13}C]glucose adequately and rapidly reached both tissues. UDP-glucose, a close metabolic derivative of glucose, was m+6 labelled at a similar magnitude in tumour and non-tumour tissues in patients and 2 out of 3 mouse models (Extended Data Fig. 3d,e). These findings are consistent with PET imaging[22], showing robust [^{18}F]fluorodeoxyglucose uptake in the cortex and GBM. Notably, lactate enrichment exceeded upstream glycolytic enrichment in both tissues (Fig. 1e,f), resembling patterns seen in lung cancer[12] and suggesting possible carbon entry into lower glycolysis through lactate uptake or exchange. To complement these LC–MS-based analyses, we also performed spatial ^{13}C-metabolite imaging of flash-frozen tissue slices using matrix-assisted laser desorption/ionization (MALDI) MS[23], which further suggested similar lactate enrichment in the cortex and most GBMs (Fig. 1g and Extended Data Fig. 4a,b). Together, these data indicate adequate ^{13}C-glucose entry into tumour and cortical tissues and similar use/exchange of labelled extracellular lactate.

GBMs rewire TCA cycle and neurotransmitter synthesis

Metabolite labelling was then examined in the TCA cycle, which oxidizes glucose-derived carbons while producing amino acids and neurotransmitters (Extended Data Fig. 3f). In the cortex, glucose-derived labelling of TCA cycle intermediates was higher than in GBM (Fig. 2a,b), indicating altered GBM TCA cycle activity and/or preferential use of non-glucose carbon sources[24–29]. To characterize temporal dynamics of TCA cycle labelling, mouse time-course [U^{13}C]glucose infusion studies were performed in which tissues were collected at multiple timepoints. In both GBM and cortex, rapid formation of m+2 TCA cycle intermediates (formed in the first TCA cycle turn) was observed. However, fractions of more complex intermediates (formed from multiple turns or a single turn involving pyruvate carboxylase) steadily increased over time only in the cortex, remaining relatively lower in GBM (Extended Data Fig. 3g–i). Isotopologue distribution changes at the latest timepoints, as GBM labelling approached steady state, also suggested trends of higher labelling in cortex than GBM (Extended Data Fig. 3j–l). These findings indicate steady, consistent glucose-derived oxidative TCA cycle turning in cortex, while asymptotic ^{13}C-labelling in GBM is consistent with a shift from physiological glucose oxidation[24–29].

TCA-cycle-derived amino acids also function as neurotransmitters or neurotransmitter precursors in the brain. In the cortex, glucose-derived carbons accounted for a substantial fraction of the neurotransmitters glutamate, gamma-aminobutyric acid (GABA), aspartate and precursor glutamine, whereas GBMs had lower ^{13}C-fractions and exhibited low GABA abundance levels almost devoid of label (Fig. 2c,d and Extended Data Fig. 2j,k). These observations were confirmed by independent MALDI-based analyses similarly revealing decreased TCA-cycle-related metabolite labelling (Fig. 2e,f and Extended Data Fig. 4c–g,i–n). To corroborate these observations, we also investigated expression of genes regulating synaptic signalling. GBM expression profiling revealed a

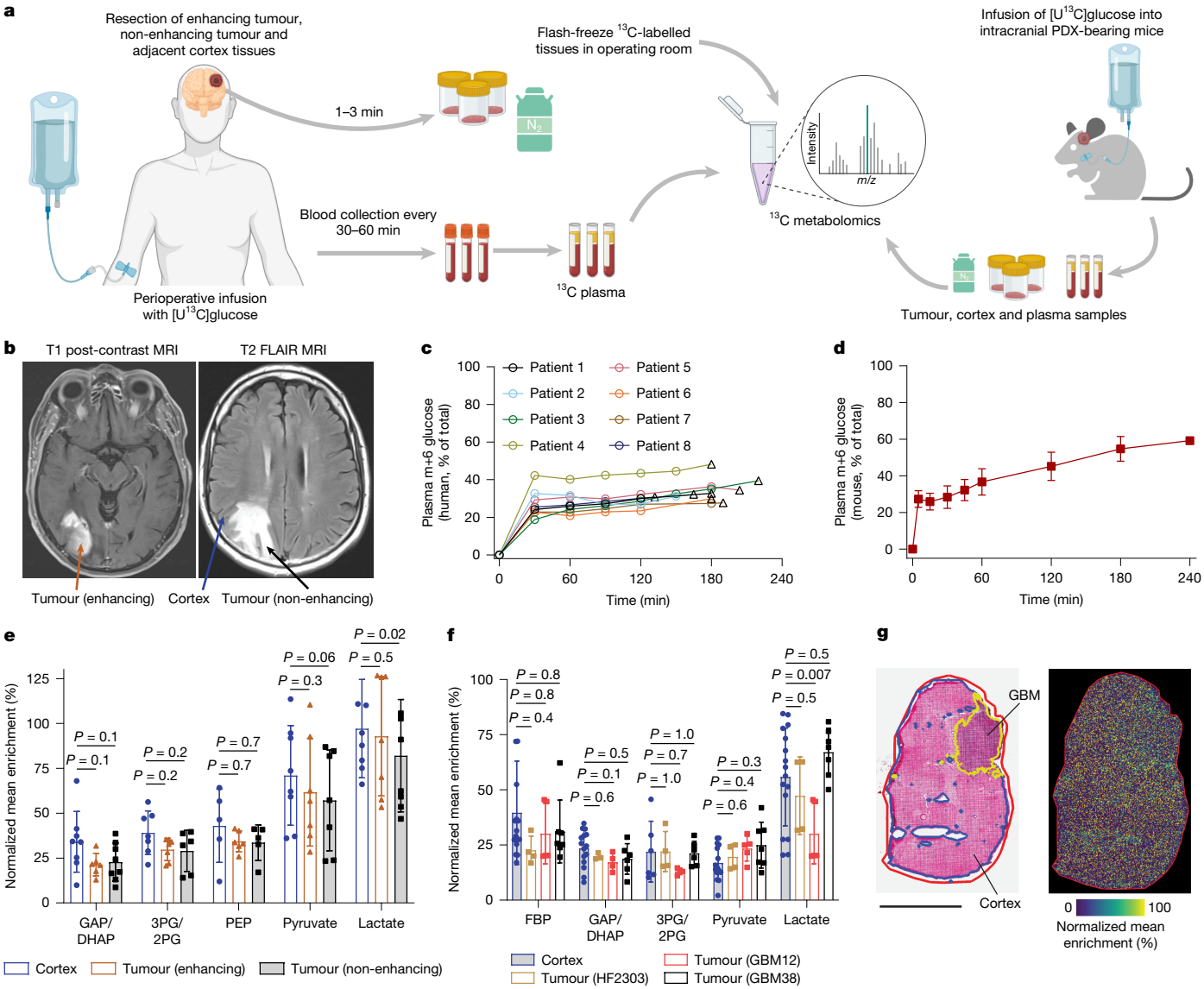

Fig. 1 | Glucose labelling of brain tumours and cortex. a, Schematic of [U^{13}C]glucose infusions and analyses of patients with glioma and patient-derived intracranial GBM mouse models. The diagram was created using BioRender. **b**, Example of magnetic-resonance-imaging-defined tissue acquisition. **c**, Arterial m+6 glucose enrichment in patients undergoing [U^{13}C]glucose infusions at the indicated times after the start of infusion. Plasma from patient 8 could not be analysed at time 0. The triangles indicate the tissue resection and flash-freezing timepoint. **d**, Arterial m+6 glucose enrichment in mice undergoing [U^{13}C]glucose infusions. Data are mean ± s.d. at each timepoint. **e**,**f**, Normalized (to labelled plasma glucose on a per-patient (**e**) or per-mouse (**f**) basis) enrichment of glycolytic intermediates in intracranial tissues from eight patients with glioma (**e**) or mouse models (**f**) infused with [U^{13}C]glucose. Data are mean ± s.d. Comparisons between groups were performed using linear mixed-effects models with a random intercept for individual. For each metabolite, multiple pairwise comparisons across tissue types were adjusted using Holm's method. Statistical tests were two-sided. **g**, H&E staining of GBM38 patient-derived xenograft (PDX) grown orthotopically (left) and MALDI image showing ^{13}C enrichment of lactate (right) with the tissue maximum set at 100%. Imaging with a separate, independent instrument was performed once and produced similar results. Scale bar, 3 mm. FBP, fructose 1,6-bisphosphate; GAP, glyceraldehyde 3-phosphate; DHAP, dihydroxyacetone phosphate; 3PG/2PG, 3-phosphoglycerate/2-phosphoglycerate; PEP, phosphoenolpyruvate.

substantial downregulation of GABA system transcripts alongside other neurotransmission genes (Extended Data Fig. 5a–e), suggesting a decrease in GABAergic inhibition and underscoring a GBM shift characterized by diminished neuroregulation and cortical identity.

GBMs activate nucleotide synthesis

GBMs exhibit [U^{13}C]glucose uptake similar to cortex but with lower TCA cycle and neurotransmitter ^{13}C labelling. To investigate alternative fates of glucose-derived carbons in GBM, we analysed metabolites that function as building blocks for macromolecules that are essential to GBM proliferation.

Nucleotides and their derivatives can be generated using glucose-derived ribose 5-phosphate (R5P) (Extended Data Fig. 3c). Purine nucleotides can be produced de novo, in which nucleobases are built on ribose, or salvaged when a preformed nucleobase is conjugated to ribose (Extended Data Fig. 3m). ^{13}C labelling of many purines increased in GBM versus in cortex (Fig. 2g,h) and, because R5P enrichment was similar between tissues (Extended Data Fig. 3n,o), the increased GBM purine labelling could probably be explained by increased biosynthesis. MALDI confirmed specific ^{13}C-purine increases in GBM (Fig. 2i and Extended Data Fig. 4h). Notably, only the GMP arm of purine synthesis was consistently enriched across patients (Extended Data Fig. 3p–v), suggesting particular importance of glioma guanylate production.

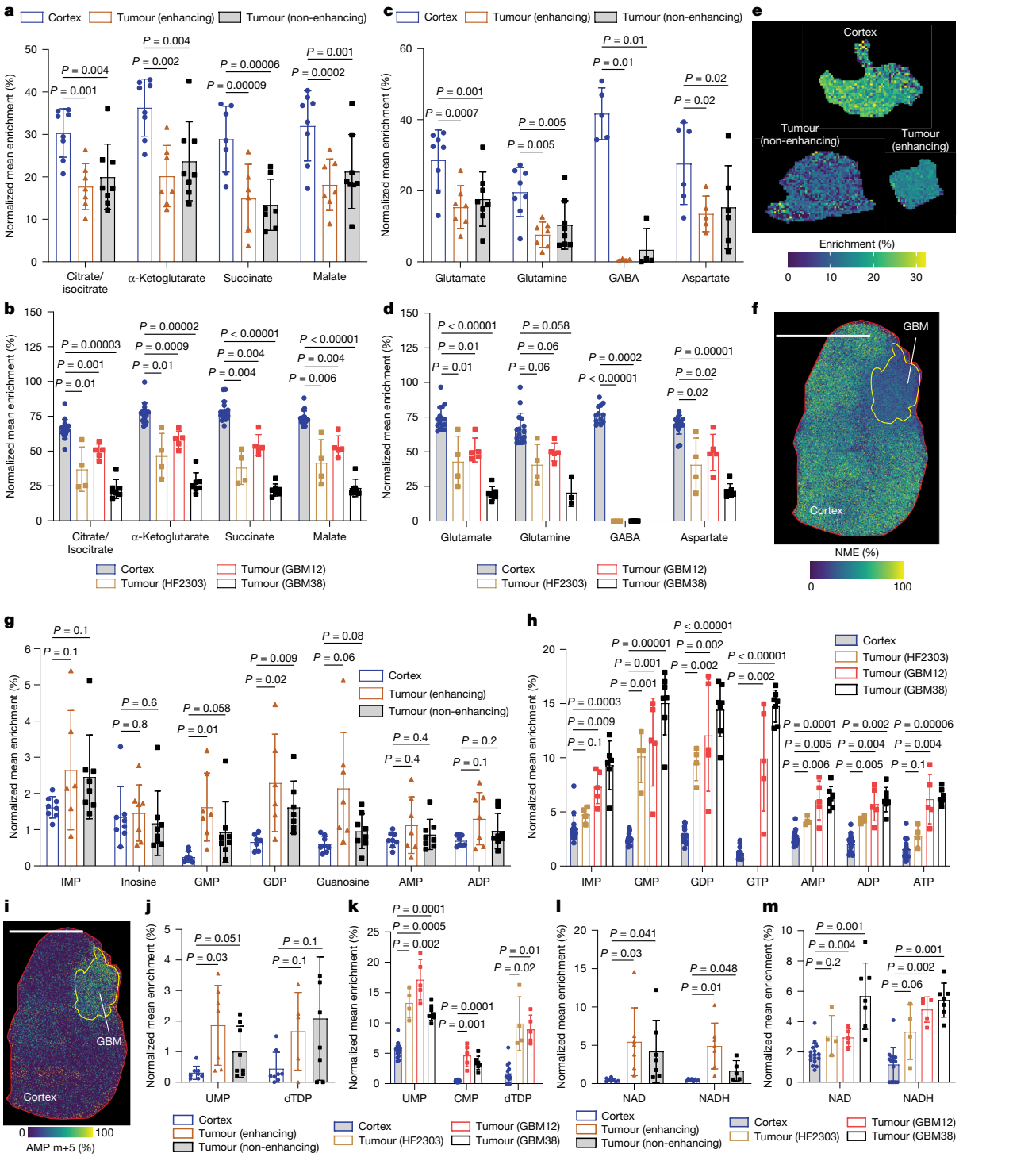

Fig. 2 | GBM modulates TCA cycle and neurotransmitters to channel glucose into nucleotides and NAD. a, Intracranial enrichment of TCA cycle intermediates in patients with glioma infused with [U^{13}C]glucose. **b**, Intracranial enrichment of TCA cycle intermediates in GBM-bearing mice infused with [U^{13}C]glucose. **c**, Intracranial enrichment of amino acids derived from the TCA cycle in patients with glioma infused with [U^{13}C]glucose. **d**, Intracranial enrichment of amino acids derived from the TCA cycle in GBM-bearing mice infused with [U^{13}C]glucose. **e**, Malate enrichment in representative human cortex, non-enhancing tumour tissue and enhancing tumour tissue. The colour bar maximum is set at true enrichment. **f**, MALDI image showing normalized mean ^{13}C enrichment of malate in brain from a GBM38 tumour-bearing mouse. GBM was defined by an overlay with H&E staining shown in Fig. 1g. The colour bar tissue maximum is normalized to 100%. Scale bar, 3 mm. **g**, Intracranial purine enrichment in patients with glioma infused with [U^{13}C]glucose. **h**, Intracranial purine enrichment in GBM-bearing mice infused with [U^{13}C]glucose. **i**, MALDI image of AMP m+5 signal intensity in brain from a GBM38 tumour-bearing mouse with tissue maximum set at 100%. GBM was defined by an overlay with H&E staining shown in Fig. 1g. Scale bar, 3 mm. **j**, Intracranial pyrimidine enrichment in patients with glioma infused with [U^{13}C]glucose. **k**, Intracranial pyrimidine enrichment in GBM-bearing mice infused with [U^{13}C]glucose. **l**, Intracranial enrichment of NAD and NADH in patients with glioma infused with [U^{13}C]glucose. **m**, Intracranial enrichment of NAD and NADH in GBM-bearing mice infused with [U^{13}C]glucose. For **a**–**d**, **g**, **h** and **j**–**m**, data are mean ± s.d. of metabolite enrichments normalized to labelled plasma glucose on a per-patient or per-mouse basis. Comparisons between groups were performed using linear mixed-effects models with a random intercept for individual, and multiple pairwise comparisons across tissue types were adjusted using Holm's method. All statistical tests were two-sided.

Like purines, pyrimidines (which also incorporate glucose-derived carbon from de novo and salvage synthesis) exhibited elevated labelling in GBM (Fig. 2j,k and Extended Data Fig. 3w–y). Glucose-derived R5P is also used to form NAD, of which redox cycling to NADH supports biosynthetic and oncogenic processes (Extended Data Fig. 3z). Consistent with increased GBM nucleotide labelling, elevated NAD and NADH labelling was also observed (Fig. 2l,m). Together, these findings suggest reprogramming of GBM glucose use from physiological activity to the biosynthetic demands of proliferation and survival, especially nucleotide synthesis.

GBM elevates nucleotide flux

As increased ^{13}C-nucleotide enrichment at a single timepoint does not necessarily imply increased flux, we developed a metabolic flux analysis (MFA) approach[30] from in vivo enrichment data (Fig. 3a) to directly quantify these fluxes and determine whether higher GBM nucleotide enrichment corresponds to higher biosynthetic flux. GBM38-bearing mice were infused with [U^{13}C]glucose, with tissues collected at multiple timepoints after infusion to generate time-dependent enrichment profiles for MFA. Nucleotide enrichment profiles showed increasing trends throughout the experiment (Extended Data Fig. 6a,b), suggesting that isotopic steady state in these pathways had yet to be achieved at tissue collection times in single-timepoint studies. To overcome this limitation, we applied an ordinary differential-equation-based MFA model using time-course nucleotide mass isotopologue distribution profiles to estimate fluxes[31], with forward and reverse fluxes included in reversible reactions (Extended Data Fig. 6c,d).

MFA revealed significant differences in nucleotide synthesis fluxes between GBM and cortex. GBMs elevated purine biosynthetic flux through de novo inosine monophosphate (IMP) and GMP synthesis, IMP and AMP salvage, and generation of inosine and guanylates (Fig. 3b). The total levels of many purines were equal or lower in abundance in GBM compared with in cortex (Extended Data Fig. 6e), highlighting that ^{13}C-MFA can provide additional pathway flux information that cannot be obtained from tracing and static metabolite levels alone. Collectively, these results indicate that higher GBM purine enrichment results from increased absolute purine biosynthesis fluxes. Pyrimidine fluxes also differed between GBM and cortex, with de novo UMP synthesis elevated in GBM and uridine salvage the dominant form of pyrimidine synthesis in both tissues (Fig. 3c).

To confirm increased de novo and salvage nucleotide production in GBM, mice were infused with pathway-specific tracers: ^{15}N-amide-glutamine was used to trace de novo nucleotides and $^{15}N_4$-inosine was used to trace purines derived from salvaged IMP. Consistent with MFA-based predictions, glutamine-derived nucleotide labelling was higher in GBM than in cortex, accompanied by elevated inosine-derived labelling of purines (Fig. 3d–f). These data align with MFA predictions based on [U^{13}C]glucose tracing that GBMs upregulate nucleotide production through de novo and salvage pathways.

GBM modulates flux after therapy

GBMs exhibit profound resistance to therapy, including standard-of-care RT, prompting us to investigate whether their metabolic adaptations could facilitate this response. GBM-bearing mice were treated with cranial RT delivered to the entire brain immediately before [U^{13}C]glucose infusions, with tissues collected at multiple timepoints after RT. Initial MFA modelling assumed metabolic steady state throughout infusion, which is unlikely to be true after RT due to rapid DNA damage response activation and cell cycle arrest. We therefore developed a dynamic ^{13}C-MFA model that incorporates time-dependent concentration changes and is used to estimate transient flux profiles[32,33] to quantify purine synthesis fluxes after RT. This framework was modified to include dynamic concentration and flux changes (Extended Data Fig. 6f–h). De novo purine fluxes changed dynamically after RT in GBM but were largely unaffected in cortex (Extended Data Fig. 7a–d). GBM de novo IMP synthesis increased transiently after treatment, with peak activity around 1 h after RT and diminishing over the next 3 h (Extended Data Fig. 7b), in alignment with the timeframe of DNA damage and repair following RT[34]. De novo GMP synthesis from IMP increased concurrently, while de novo AMP synthesis decreased (Extended Data Fig. 7c,d). Other pathways remained stable in both tissues (Extended Data Fig. 7e–r), suggesting that GBM selectively rewires de novo purine synthesis in response to RT. Collectively these data suggest that, after RT, GBMs acutely increase de novo IMP synthesis and channel it towards GMP production while reducing AMP synthesis.

These findings were validated by infusing GBM-bearing mice with $^{15}N_4$-inosine or ^{15}N-amide-glutamine after RT. Consistent with MFA, RT did not affect IMP salvage from hypoxanthine or inosine (Extended Data Fig. 7s). GMP salvage from guanine could not be directly assessed due to low circulation enrichment[35]. In mice infused with ^{15}N-glutamine, the abundance of m+3 GMP (reflecting de novo IMP origin, not guanine) was higher in RT-treated GBM compared with in the controls (Extended Data Fig. 7t), consistent with increased GMP synthesis from IMP after RT. IMP and AMP changes after RT could not be identified, probably because the longer infusion times required for intracranial ^{15}N-tracer accumulation did not assess predicted early transient shifts (Extended Data Fig. 7u,v). To the best of our knowledge, these findings represent the first intracranial measurements of purine synthesis after RT in GBM. Increased de novo purine synthesis in vivo is consistent with heightened GBM guanylate dependence after RT[7] and is currently under investigation as a radiosensitization target (NCT04477200, NCT05236036).

GBM prioritizes serine uptake

De novo purine synthesis uses several amino acids, including serine, which is also a precursor for glycine and one-carbon units (especially in nucleotide-demanding proliferating T cells[36]), a driver of lipid synthesis and a neuromodulator in its D-racemized configuration. Serine, which can be synthesized from glucose and is non-essential in normal tissues, can drive the growth and aggressiveness of tumours including GBM[37–42], prompting additional analysis to better understand its metabolism in GBM.

Total serine labelling was similar in glioma and cortex (Extended Data Fig. 8a,b), distinct from other amino acids, neurotransmitters and nucleotides, which exhibited differential label enrichment (Fig. 2). Deeper analysis of serine labels revealed that m+3 serine was higher in cortex than in enhancing tumour tissue in nearly every patient, while m+1 serine was predominant in most gliomas (Extended Data Fig. 8c,d). This shift became even more evident when labelling across individuals was standardized by ratios of those isotopologues (Fig. 4a and Extended Data Fig. 8e). Parallel labelling patterns were observed in mice, in which m+3 serine was higher in cortex than in GBM, and m+1 serine was predominant in GBM (Fig. 4b and Extended Data Fig. 8f). Predominance of m+1 serine has been observed in previous human cancer [U^{13}C]glucose infusion studies[11,26,43] (Extended Data Fig. 8g–k), although the finding is of uncertain significance. Although cortex has not been analysed in other human tracing studies, the brain is one of the few organs in [U^{13}C]glucose-infused mice in which m+3 serine labelling approximates m+1 labelling[26] (Extended Data Fig. 8l), consistent with our results. These previous findings support the labelling patterns observed in experiments reported here.

Labelled serine can be acquired through glucose-derived de novo synthesis, production from a folate cycle carbon and glycine, or environmental uptake. As the glycolytic intermediate and serine precursor phosphoglycerate was predominantly m+3 labelled in GBM and cortex (Extended Data Fig. 8m,n), any intracranial serine formed de novo from glycolysis would also be predominantly m+3 labelled. The predominance of m+3 serine in cortex and m+1 serine in glioma suggested cortex

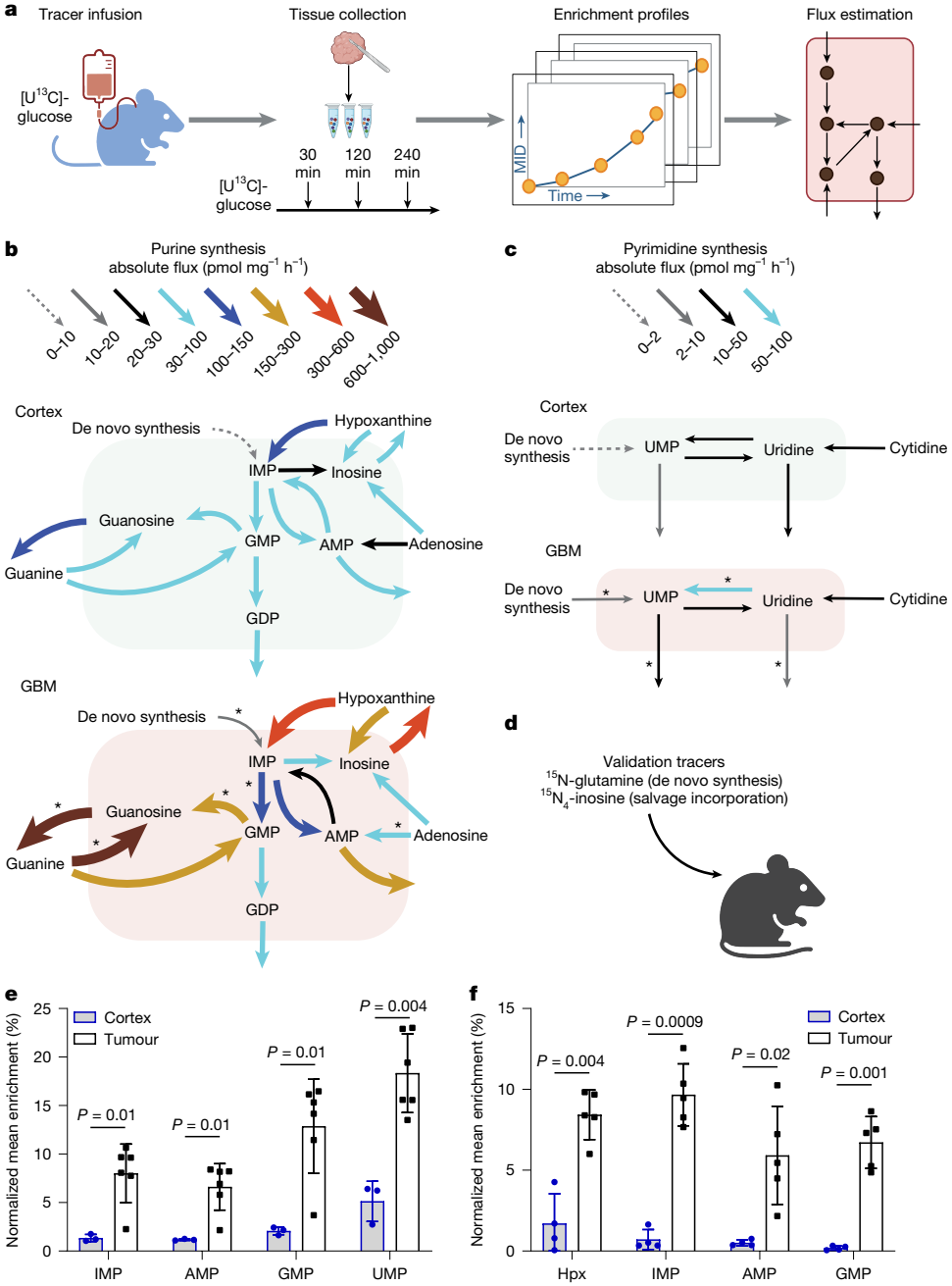

Fig. 3 | GBM elevates nucleotide biosynthesis fluxes. a, Flux estimation scheme: to measure metabolite enrichment and estimate metabolic fluxes, analysis was performed using GBM and cortex tissues from intracranial GBM38-bearing mice infused with [U^{13}C]glucose that were serially euthanized at varying timepoints (0, 30, 120 and 240 min). **b**, Purine synthesis fluxes in mouse cortex and orthotopic GBM38 tissues calculated from [U^{13}C]glucose MFA. Statistical significance was determined by non-overlapping 95% confidence intervals; *$P < 0.05$. **c**, Pyrimidine synthesis fluxes in mouse cortex and orthotopic GBM38 tissues calculated from [U^{13}C]glucose MFA. Statistical significance was determined by non-overlapping 95% confidence intervals. **d**, Validation of [U^{13}C]glucose MFA through stable isotope labelling experiments comparing labelling of tumour and cortex tissues from intracranial GBM38-bearing mice infused with either ^{15}N-amide-glutamine or ^{15}N$_4$-inosine. **e**, Normalized (to labelled plasma glutamine on a per-mouse basis) enrichment of nucleotides in cortex and orthotopic tumour tissue from intracranial GBM38-bearing mice infused with ^{15}N-amide-glutamine. Data are mean ± s.d. of cortex and tumour samples isolated from three mice containing one to three intracranial tumour foci each. Comparisons between groups were performed using linear mixed-effects models with a random intercept for mouse. Tests were two-sided. **f**, Normalized (to labelled plasma inosine on a per-mouse basis) enrichment of purines in cortex and orthotopic tumour tissue from intracranial GBM38-bearing mice infused with ^{15}N$_4$-inosine. Data are mean ± s.d. of cortex and tumour samples from four mice containing one to two tumour foci each. Comparisons between groups were performed using linear mixed-effects models with a random intercept for mouse. Tests were two-sided. Hpx, hypoxanthine; MID, mass isotopologue distribution. The diagrams in **a** and **d** were created using BioRender.

primarily generates serine from glucose while GBM tissue probably relied on other sources.

Arterial serine was almost exclusively m+1 labelled (Extended Data Fig. 8m,n), probably due to synthesis from unlabelled glycine and a labelled folate carbon. This indicated higher m+1 serine in GBM could be explained by increased uptake of circulating serine. However, intracranial m+1 serine could also arise from direct synthesis using unlabelled glycine and labelled one-carbon units in the folate cycle. Given this

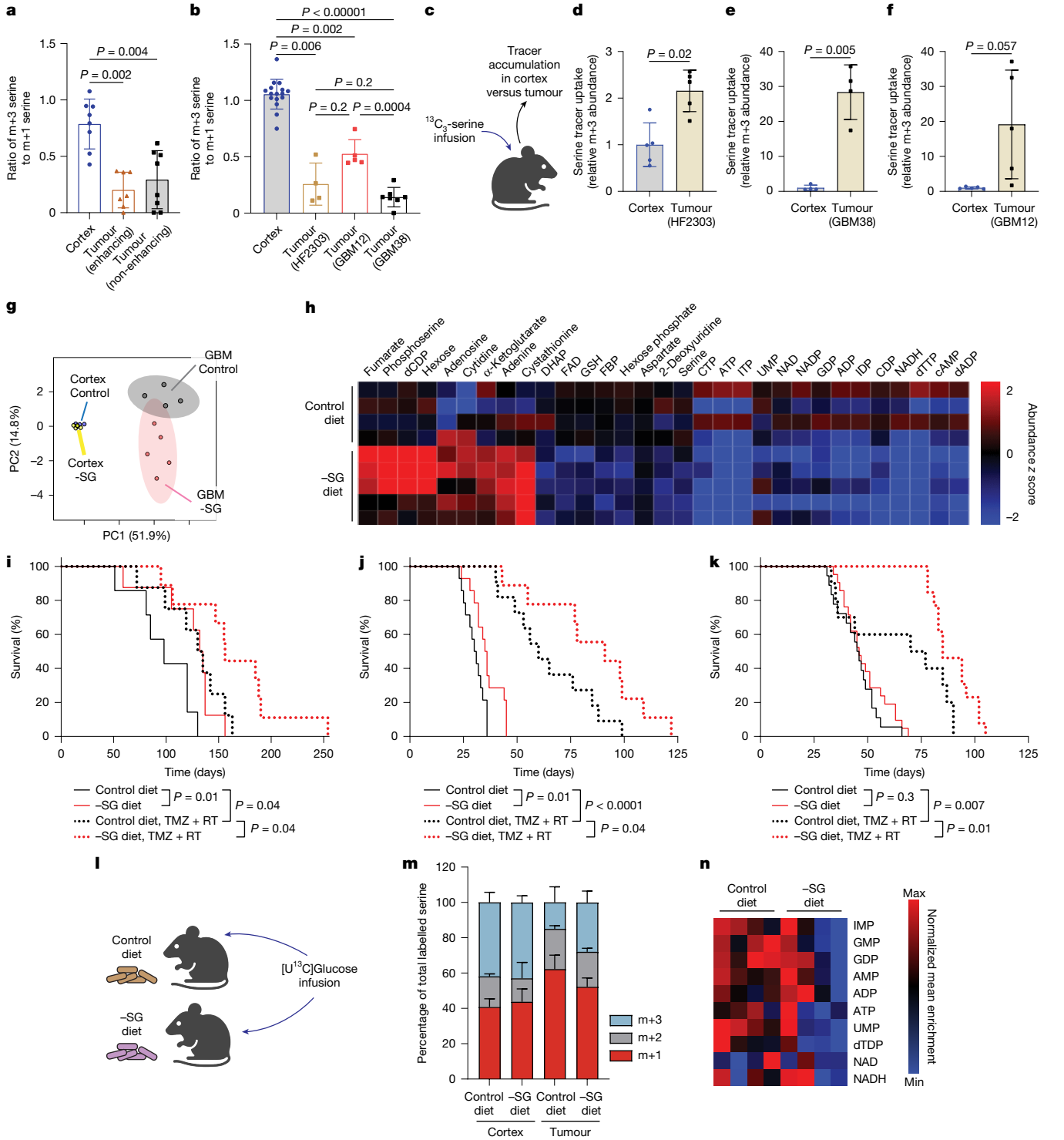

Fig. 4 | Rewired serine metabolism enables GBM nucleotides and therapeutic resistance that can be overcome by dietary serine/glycine restriction. **a**,**b**, The ratios of m+3 serine to m+1 serine in cortex and tumour tissues from patients with glioma (**a**) or intracranial GBM-bearing mice (**b**) infused with [U^{13}C]glucose. Data are mean ± s.d. Comparisons between groups were performed using linear mixed-effects models with a random intercept for individual, and multiple pairwise comparisons across tissue types were adjusted using Holm's method. All statistical tests were two-sided. **c**, $^{13}C_3$-serine (m+3) was infused into orthotopic GBM-bearing mice to compare serine uptake between cortex and intracranial GBM. **d**–**f**, The relative accumulation of infused m+3 serine into mouse cortex and intracranial HF2303 (**d**), GBM38 (**e**) or GBM12 (**f**) tumours. Data are mean ± s.d. Groups were compared using two-sided *t*-tests. **g**, Principal component analysis of metabolite levels from cortex and intracranial GBM38 tissues from mice on control diets or –SG diets. **h**, The relative metabolite levels (top PLS-DA) in orthotopic GBM38 tumours from mice fed control or –SG diets; each row represents a separate tumour. **i**–**k**, The survival of intracranial HF2303 (**i**), GBM38 (**j**) and GBM12 (**k**) tumour-bearing mice under altered dietary serine/glycine conditions alone or in combination with chemoradiation treatment. Two-sided log-rank tests were performed to compare survival curves between groups. **l**, Intracranial tumour-bearing mice on control diets or –SG diets were infused with [U^{13}C] glucose and assessed for metabolite labelling. **m**, Isotopologue distributions of labelled serine in intracranial HF2303 tumour-bearing mice infused with [U^{13}C]glucose. Data are mean ± s.d. **n**, Normalized (to labelled plasma glucose on a per-mouse basis) enrichment of nucleotides and NAD species in HF2303 tumours from intracranial GBM-bearing mice infused with [U^{13}C]glucose. The diagrams in **c** and **l** were created using BioRender.

complexity, we developed a multicompartment ^{13}C-MFA model to understand the relative magnitudes of these fluxes (Extended Data Fig. 8o) and calculate scores for ratios of serine de novo synthesis flux to uptake flux. Mouse cortex predominantly relied on de novo serine synthesis while 2 out of the 3 GBM models (HF2303, GBM38) derived most serine from extracellular sources (Extended Data Fig. 8p). Patient samples similarly exhibited some heterogeneity. While cortex predominantly generated serine de novo, many tumour samples (11 out of 15 enhancing/non-enhancing) primarily relied on extracellular serine uptake (Extended Data Fig. 8p,q). Together, these data indicated that the relative flux of de novo serine synthesis is lower in many gliomas than cortex, and that gliomas scavenge serine from the environment.

To validate these inferences from [U^{13}C]glucose tracing, exogenous serine uptake was directly traced in GBM-bearing mice. Mice were infused with $^{13}C_3$-serine (m+3) into the circulation, and tracer accumulation into cortex and GBM tissue was measured, whereby tissue levels of m+3 serine indicate acquisition from extracellular sources. In all three models, GBM accumulated more m+3 serine from plasma compared with cortex (Fig. 4c–f), confirming that GBMs have increased environmental serine uptake.

While direct ^{13}C-serine-tracing experiments revealed higher GBM serine uptake than cortex in all models, the ^{13}C-glucose MFA indicated that the ratios of de novo synthesis versus uptake of serine vary across gliomas. This suggests that, while elevated serine uptake is common in GBM, increased glucose-driven serine synthesis may be limited to certain tumours. Given the heightened serine demand indicated by both methods, we investigated the expression of genes related to serine metabolism between tumour and cortex. Archived RNA-sequencing (RNA-seq) data suggested increased expression of the serine-synthesis enzyme phosphoserine phosphatase and a variety of serine transporters in GBM (Extended Data Fig. 5f–h). Patient-specific tumour heterogeneity, functional redundancy of multiple serine transporters[44] and transport of multiple amino acids are likely to contribute to variability based on individual tumour metabolic demands.

Serine restriction enhances GBM therapy

The experiments above suggested that many gliomas prioritize serine uptake over glucose-derived synthesis, enabling them to allocate glucose carbons towards other biosynthetic needs. In such a scenario, depleting environmental serine would force GBMs to increase glucose-derived serine synthesis at the expense of glucose-derived nucleotide production required for aggressive phenotypes. To test this hypothesis, patient-derived gliomaspheres were grown in serine- and glycine-depleted medium followed by tracing of [U^{13}C]glucose into serine. Medium serine/glycine restriction reduced intracellular serine, with remaining serine predominantly glucose derived (Extended Data Fig. 9a,b). Nucleotides were also broadly reduced (Extended Data Fig. 9c), indicating that GBMs depend on exogenous serine to channel glucose carbons into biosynthesis. These findings suggest that, without extracellular serine, gliomaspheres cannot fully compensate through de novo synthesis despite ample glucose, exposing a metabolic bottleneck and highlighting their reliance on environmental serine.

To determine whether exogenous serine restriction alters GBM metabolism intracranially, we performed experiments with tumour-bearing mice fed a control diet or a diet lacking serine and glycine (−SG). The −SG diet decreased circulating serine levels (Extended Data Fig. 10a) and was well tolerated. While mice on the −SG diet long term exhibited mild to moderate growth delays, blood cell counts and standard blood chemistries were minimally affected (Extended Data Fig. 10b–x); no other behavioural or functional consequences were noted. The −SG diet altered GBM metabolomes with little effect on cortical metabolites (Fig. 4g,h and Extended Data Fig. 9d), consistent with glucose-driven de novo serine synthesis predominating in cortex. GBMs from mice on the −SG diet had lower serine and nucleotides compared with the controls and higher levels of phosphoserine (Fig. 4h and Extended Data Fig. 9e), formed when glucose carbons are shunted towards serine.

The finding that environmental serine restriction selectively altered GBM metabolism suggested that the −SG diet might reduce GBM growth. Having identified widespread increased serine uptake and heterogeneous serine synthesis in GBM, we examined whether serine-depletion phenotypes corresponded to baseline use of de novo serine synthesis versus uptake. When mice were restricted for environmental serine, tumours with high serine uptake/synthesis ratios (HF2303, GBM38) were smaller than controls and had lower Ki-67/proliferation indices (Extended Data Fig. 11a–f). Dietary serine restriction improved the survival times of HF2303 and GBM38 tumour-bearing mice (Fig. 4i,j). By contrast, GBM12 tumours, with higher glucose-derived serine synthesis (Fig. 4b and Extended Data Fig. 8f,p), exhibited no changes in growth or Ki-67 in serine-restricted mice (Extended Data Fig. 11g–i), nor were the survival times affected by the −SG diet (Fig. 4k). These results suggest that GBMs with low serine synthesis rely on environmental serine that can be targeted by dietary serine restriction.

Chemoradiation is the current standard-of-care GBM treatment and amplifies tumour biosynthetic demand[7,8]. This increased purine reliance could heighten demand for exogenous serine, serving as a precursor and potentially enabling glucose to be redirected from serine synthesis toward nucleotide production. To determine whether −SG diets increase chemoradiation efficacy, mice receiving control or −SG diets were treated with RT and TMZ (Extended Data Fig. 11j–l). While −SG diet monotherapy effects were selective to certain GBMs, the −SG diet improved chemoradiation efficacy across models (Fig. 4i–k). This suggests GBMs are selectively sensitive to serine deprivation at the baseline but, under conditions of genomic and biosynthetic stress, they cannot adapt to environmental serine restriction.

These data suggested many GBMs upregulate capture of alternative carbon sources, such as serine, to preferentially reroute glucose-derived carbon into biomass production. To validate this carbon partitioning model, we infused [U^{13}C]glucose into GBM-bearing mice fed control or −SG diets. In HF2303 tumours, which exhibited limited glucose-driven serine synthesis (Fig. 4b and Extended Data Fig. 8p) and responded favourably to dietary serine deprivation (Fig. 4i), the −SG diet increased glucose-driven serine synthesis (m+3 serine), an effect that was not observed in cortex (Fig. 4l,m). Serine-restricted diets decreased GBM glucose-derived nucleotide labelling (Fig. 4n), exhibiting lower ratios of glucose-derived nucleotides to glycolysis-derived serine compared with the controls (Extended Data Fig. 9f–i). A similar experiment was performed using mice with GBM12 tumours, which derive more serine from glucose than other models and are less sensitive to dietary serine restriction (Fig. 4b,k and Extended Data Fig. 8p). In this model, the −SG diet did not alter glucose-driven serine or nucleotide labelling (Extended Data Fig. 9j–o). Together, these data reveal that many gliomas preferentially depend on extracellular serine, yet can adapt to restriction by curbing proliferation and redirecting glucose carbons from biomass production to serine synthesis—a vulnerability that can be leveraged to enhance the efficacy of chemoradiation (Fig. 5).

Discussion

Here we used clinical stable isotope infusions and MFA to define brain cancer metabolic rewiring and its therapeutic implications. While both GBM and cortex avidly consume glucose, cortex predominantly uses glucose-derived carbons for physiological processes such as TCA cycle oxidation and neurotransmitter synthesis. GBMs downregulate these physiological processes and instead use glucose-derived carbons to synthesize nucleotides, fuelling proliferation and treatment resistance. Many gliomas also upregulate environmental serine acquisition, while the cortex synthesizes a higher fraction of its serine from glucose. This metabolic rewiring is a targetable liability with a therapeutic window.

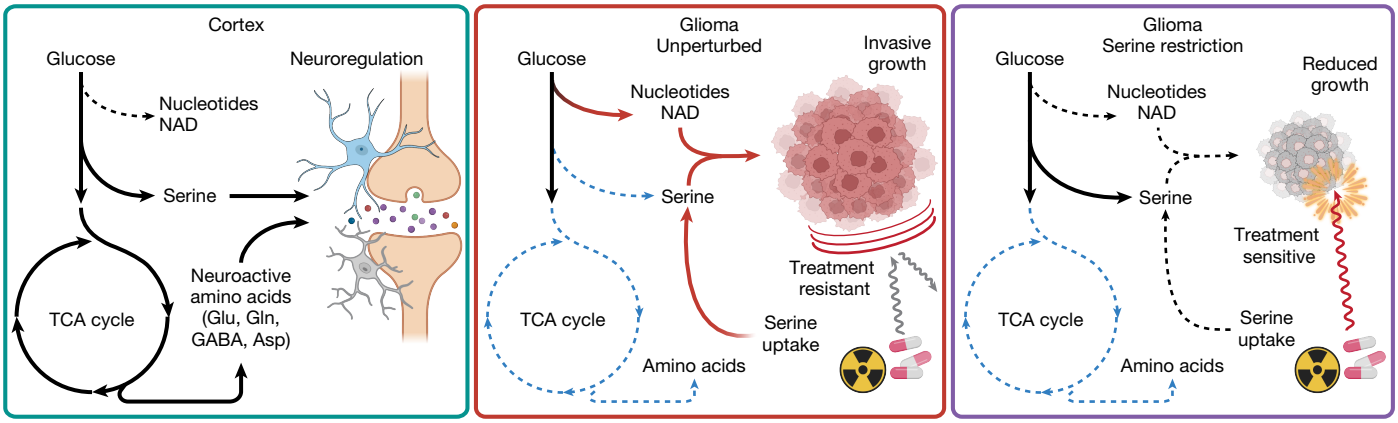

Fig. 5 | Reprogramming of cortical glucose metabolism fuels GBM growth and therapy resistance. Models of cortical metabolic rewiring in brain cancer: cortex (left) robustly takes up glucose, which it uses to fuel the TCA cycle and synthesize neuroregulatory metabolites including serine, glutamate, glutamine, GABA and aspartate. Brain tumours (middle) upregulate the uptake of environmental serine and reduce the fraction of glucose incorporated into the TCA cycle and glucose-derived neurotransmitter synthesis. Tumours also reroute glucose-derived carbons to synthesize nucleotides and NAD/NADH, used to drive tumour growth and resistance to chemoradiation. Restriction of dietary serine (right) forces multiple gliomas to reroute glucose carbon towards serine synthesis, which decreases nucleotide and NAD/NADH levels, slows tumour growth and sensitizes tumours to chemoradiation. The diagram was created using BioRender.

In mouse models, dietary serine restriction depletes GBM nucleotides and slows tumour growth while minimally affecting cortex metabolites.

This study adds to our growing understanding of metabolic rewiring in cancer. Like radioactive glucose analogues used in PET, [U^{13}C]glucose rapidly accumulates in both GBM and cortex[22], which suggests that broadly targeting glucose uptake may cause untoward toxicity. Like previous ^{13}C-labelling studies, we find an active TCA cycle in brain cancer[13,14,45,46]. However, our unique surgical practice enabled us to compare metabolism in human cortex and brain cancer, showing that the TCA cycle is altered in GBM compared with non-malignant cortex, with decreased glucose-derived labelling suggesting either reduced activity or increased reliance on non-glucose substrates[13,28,29]. To our knowledge, serine synthesis routes have not previously been examined in human cancer. In contrast to brain metastases[41] and cortex, which appear to rely on de novo serine synthesis in preclinical models[41], many gliomas preferentially rely on environmental serine and can therefore use glucose-derived carbon for other purposes.

Our flux models and subsequent validation provide insights into metabolic rewiring that are difficult to glean with simpler analysis techniques[30,31,47–49]. While de novo synthesis of nucleotides is elevated in GBM compared with in cortex, salvage of uridine and hypoxanthine appears to dominate nucleotide production. This contrasts with other brain tumours in which de novo pyrimidine synthesis is critical[50–52]. GBMs also appear to adaptively rewire metabolism, particularly GMP synthesis, in response to RT, which may contribute to treatment resistance. The development of single-timepoint flux models will hopefully help translate these tools to clinical practice, where time-course sample acquisition can be impractical.

Our work has important clinical implications. Inhibiting nucleotide synthesis, serine uptake or non-glucose TCA cycle fuel sources might have a therapeutic index to selectively affect GBM, whereas broadly targeting glucose uptake may cause unacceptable cortical toxicity. Targeting proximal de novo nucleotide synthesis in GBM may be ineffective due to active salvage pathways. Blocking IMPDH may still have a therapeutic benefit in glioma with a favourable therapeutic ratio owing to the preference for gliomas to salvage hypoxanthine. Restricting dietary serine could help to slow GBM growth and potentially augment the efficacy of standard-of-care GBM treatments[53], although the efficacy of this approach could be limited by local production of serine in the GBM microenvironment[54]. The patient-to-patient heterogeneity in environmental serine dependence we observed suggests that isotope tracing could be used as a precision medicine technique to determine which patients could benefit from dietary serine restriction.

Our studies provide insights into potential strategies to target serine metabolism in brain tumours. Mouse modelling and isotope tracing suggest that tumours with the lowest levels of glucose-driven serine synthesis will be most sensitive to environmental serine depletion. Depleting environmental serine in humans is achievable through specialized diets already in the clinic (NCT05078775), although other depletion strategies could be used in the future[55,56]. In our mouse models, dietary serine deprivation reduced circulating serine levels by 25%, which may be related to the mouse strain used[57–59]. Given the upregulation of numerous putative serine transporters in gliomas, environmental serine depletion may be more efficacious than pharmacological transporter inhibition. Finally, our mouse studies suggest pairing environmental serine depletion with chemoradiation could maximize efficacy, and we are now designing a trial to test these combinations in the clinic.

Our study also lays the groundwork for future investigation. Expanding the use of isotope tracing beyond the small number of patients with brain cancer in this study will help us to understand the links between metabolism and genotype, treatment responses and prognosis. Using tracers beyond glucose will help us to understand additional aberrant metabolic pathways in cancer. While our studies required analysis of bulk tissues, future advances in technologies such as spatial metabolomics could improve the understanding of metabolic dysregulation in discrete GBM cell types including growth-promoting myeloid cells[60].

In summary, we have identified profound growth-promoting rewiring of glucose metabolism in aggressive human brain cancers. These cancer-specific metabolic alterations are compelling targets with favourable therapeutic indices. Our research team and others are currently inhibiting these metabolic pathways in patients with brain cancer (NCT04477200, NCT05236036). We are hopeful that broader use of isotope tracing in clinical studies will help us to make additional fundamental observations about cancer metabolism and teach us which patients might benefit most from metabolically targeted therapies.

Online content

Any methods, additional references, Nature Portfolio reporting summaries, source data, extended data, supplementary information, acknowledgements, peer review information; details of author contributions

and competing interests; and statements of data and code availability are available at https://doi.org/10.1038/s41586-025-09460-7.

1. Mergenthaler, P., Lindauer, U., Dienel, G. A. & Meisel, A. Sugar for the brain: the role of glucose in physiological and pathological brain function. *Trends Neurosci.* **36**, 587–597 (2013).
2. Patel, A. P. et al. Single-cell RNA-seq highlights intratumoral heterogeneity in primary glioblastoma. *Science* **344**, 1396–1401 (2014).
3. Yabo, Y. A., Niclou, S. P. & Golebiewska, A. Cancer cell heterogeneity and plasticity: a paradigm shift in glioblastoma. *Neuro Oncol.* **24**, 669–682 (2022).
4. Stupp, R. et al. Effects of radiotherapy with concomitant and adjuvant temozolomide versus radiotherapy alone on survival in glioblastoma in a randomised phase III study: 5-year analysis of the EORTC-NCIC trial. *Lancet Oncol.* **10**, 459–466 (2009).
5. Cancer Genome Atlas Research Network. Comprehensive genomic characterization defines human glioblastoma genes and core pathways. *Nature* **455**, 1061–1068 (2008).
6. Scott, A. J., Lyssiotis, C. A. & Wahl, D. R. Clinical targeting of altered metabolism in high-grade glioma. *Cancer J.* **27**, 386–394 (2021).
7. Zhou, W. et al. Purine metabolism regulates DNA repair and therapy resistance in glioblastoma. *Nat. Commun.* **11**, 3811 (2020).
8. Shireman, J. M. et al. De novo purine biosynthesis is a major driver of chemoresistance in glioblastoma. *Brain* **144**, 1230–1246 (2021).
9. Wu, X. et al. Threonine fuels glioblastoma through YRDC-mediated codon-biased translational reprogramming. *Nat. Cancer* **5**, 1024–1044 (2024).
10. Langleben, D. D. & Segall, G. M. PET in differentiation of recurrent brain tumor from radiation injury. *J. Nucl. Med.* **41**, 1861–1867 (2000).
11. Courtney, K. D. et al. Isotope tracing of human clear cell renal cell carcinomas demonstrates suppressed glucose oxidation in vivo. *Cell Metab.* **28**, 793–800 (2018).
12. Hensley, C. T. et al. Metabolic heterogeneity in human lung tumors. *Cell* **164**, 681–694 (2016).
13. Mashimo, T. et al. Acetate is a bioenergetic substrate for human glioblastoma and brain metastases. *Cell* **159**, 1603–1614 (2014).
14. Maher, E. A. et al. Metabolism of [U-13C]glucose in human brain tumors in vivo. *NMR Biomed.* **25**, 1234–1244 (2012).
15. Gerritsen, J. K. W. et al. Safe surgery for glioblastoma: recent advances and modern challenges. *Neurooncol. Pract.* **9**, 364–379 (2022).
16. Berezovsky, A. D. et al. Sox2 promotes malignancy in glioblastoma by regulating plasticity and astrocytic differentiation. *Neoplasia* **16**, 193–206 (2014).
17. Ye, L. F. et al. Patient-derived glioblastoma cultures as a tool for small-molecule drug discovery. *Oncotarget* **11**, 443–451 (2020).
18. Al-Holou, W. N. et al. Subclonal evolution and expansion of spatially distinct THY1-positive cells is associated with recurrence in glioblastoma. *Neoplasia* **36**, 100872 (2023).
19. Vaubel, R. A. et al. Genomic and phenotypic characterization of a broad panel of patient-derived xenografts reflects the diversity of glioblastoma. *Clin. Cancer Res.* **26**, 1094–1104 (2020).
20. Tong, Z., Yamaki, T., Harada, K. & Houkin, K. In vivo quantification of the metabolites in normal brain and brain tumors by proton MR spectroscopy using water as an internal standard. *Magn. Reson. Imaging* **22**, 1017–1024 (2004).
21. Chinnaiyan, P. et al. The metabolomic signature of malignant glioma reflects accelerated anabolic metabolism. *Cancer Res.* **72**, 5878–5888 (2012).
22. Hustinx, R., Smith, R. J., Benard, F., Bhatnagar, A. & Alavi, A. Can the standardized uptake value characterize primary brain tumors on FDG-PET? *Eur. J. Nucl. Med. Mol. Imaging* **26**, 1501–1509 (1999).
23. Wang, L. et al. Spatially resolved isotope tracing reveals tissue metabolic activity. *Nat. Methods* **19**, 223–230 (2022).
24. Hui, S. et al. Glucose feeds the TCA cycle via circulating lactate. *Nature* **551**, 115–118 (2017).
25. Fan, J. et al. Glutamine-driven oxidative phosphorylation is a major ATP source in transformed mammalian cells in both normoxia and hypoxia. *Mol. Syst. Biol.* **9**, 712 (2013).
26. Hui, S. et al. Quantitative fluxomics of circulating metabolites. *Cell Metab.* **32**, 676–688 (2020).
27. Yang, C. et al. Glutamine oxidation maintains the TCA cycle and cell survival during impaired mitochondrial pyruvate transport. *Mol. Cell* **56**, 414–424 (2014).
28. Comerford, S. A. et al. Acetate dependence of tumors. *Cell* **159**, 1591–1602 (2014).
29. Schug, Z. T. et al. Acetyl-CoA synthetase 2 promotes acetate utilization and maintains cancer cell growth under metabolic stress. *Cancer Cell* **27**, 57–71 (2015).
30. Achreja, A. et al. Metabolic collateral lethal target identification reveals MTHFD2 paralogue dependency in ovarian cancer. *Nat. Metab.* **4**, 1119–1137 (2022).
31. Zhu, Z. et al. Tumour-reprogrammed stromal BCAT1 fuels branched-chain ketoacid dependency in stromal-rich PDAC tumours. *Nat. Metab.* **2**, 775–792 (2020).
32. Leighty, R. W. & Antoniewicz, M. R. Dynamic metabolic flux analysis (DMFA): a framework for determining fluxes at metabolic non-steady state. *Metab. Eng.* **13**, 745–755 (2011).
33. Martinez, V. S., Buchsteiner, M., Gray, P., Nielsen, L. K. & Quek, L. E. Dynamic metabolic flux analysis using B-splines to study the effects of temperature shift on CHO cell metabolism. *Metab. Eng. Commun.* **2**, 46–57 (2015).
34. Markova, E., Schultz, N. & Belyaev, I. Y. Kinetics and dose-response of residual 53BP1/gamma-H2AX foci: co-localization, relationship with DSB repair and clonogenic survival. *Int. J. Radiat. Biol.* **83**, 319–329 (2007).
35. Tran, D. H. et al. De novo and salvage purine synthesis pathways across tissues and tumors. *Cell* **187**, 3602–3618 (2024).
36. Ma, E. H. et al. Serine is an essential metabolite for effector T cell expansion. *Cell Metab.* **25**, 345–357 (2017).
37. Mattaini, K. R., Sullivan, M. R. & Vander Heiden, M. G. The importance of serine metabolism in cancer. *J. Cell Biol.* **214**, 249–257 (2016).
38. Maddocks, O. D. et al. Serine starvation induces stress and p53-dependent metabolic remodelling in cancer cells. *Nature* **493**, 542–546 (2013).
39. Engel, A. L. et al. Serine-dependent redox homeostasis regulates glioblastoma cell survival. *Br. J. Cancer* **122**, 1391–1398 (2020).
40. Pacold, M. E. et al. A PHGDH inhibitor reveals coordination of serine synthesis and one-carbon unit fate. *Nat. Chem. Biol.* **12**, 452–458 (2016).
41. Ngo, B. et al. Limited environmental serine and glycine confer brain metastasis sensitivity to PHGDH inhibition. *Cancer Discov.* **10**, 1352–1373 (2020).
42. Kim, D. et al. SHMT2 drives glioma cell survival in ischaemia but imposes a dependence on glycine clearance. *Nature* **520**, 363–367 (2015).
43. Johnston, K. et al. Isotope tracing reveals glycolysis and oxidative metabolism in childhood tumors of multiple histologies. *Med* **2**, 395–410 (2021).
44. Butler, M., van der Meer, L. T. & van Leeuwen, F. N. Amino acid depletion therapies: starving cancer cells to death. *Trends Endocrinol. Metab.* **32**, 367–381 (2021).
45. Schwaiger-Haber, M. et al. Using mass spectrometry imaging to map fluxes quantitatively in the tumor ecosystem. *Nat. Commun.* **14**, 2876 (2023).
46. Marin-Valencia, I. et al. Analysis of tumor metabolism reveals mitochondrial glucose oxidation in genetically diverse human glioblastomas in the mouse brain in vivo. *Cell Metab.* **15**, 827–837 (2012).
47. Mittal, A. et al. Radiotherapy-induced metabolic hallmarks in the tumor microenvironment. *Trends Cancer* **8**, 855–869 (2022).
48. Achreja, A., Meurs, N. & Nagrath, D. Quantifying metabolic transfer mediated by extracellular vesicles using Exo-MFA: an integrated empirical and computational platform. *Methods Mol. Biol.* **2088**, 205–221 (2020).
49. Achreja, A. et al. Exo-MFA—a 13C metabolic flux analysis framework to dissect tumor microenvironment-secreted exosome contributions towards cancer cell metabolism. *Metab. Eng.* **43**, 156–172 (2017).
50. Shi, D. D. et al. De novo pyrimidine synthesis is a targetable vulnerability in IDH mutant glioma. *Cancer Cell* **40**, 939–956 (2022).
51. Gwynne, W. D. et al. Cancer-selective metabolic vulnerabilities in MYC-amplified medulloblastoma. *Cancer Cell* **40**, 1488–1502 (2022).
52. Pal, S. et al. A druggable addiction to de novo pyrimidine biosynthesis in diffuse midline glioma. *Cancer Cell* **40**, 957–972 (2022).
53. Falcone, M. et al. Sensitisation of cancer cells to radiotherapy by serine and glycine starvation. *Br. J. Cancer* **127**, 1773–1786 (2022).
54. Zhang, D. et al. PHGDH-mediated endothelial metabolism drives glioblastoma resistance to chimeric antigen receptor T cell immunotherapy. *Cell Metab.* **35**, 517–534 (2023).
55. Juluri, K. R., Siu, C. & Cassaday, R. D. Asparaginase in the treatment of acute lymphoblastic leukemia in adults: current evidence and place in therapy. *Blood Lymphat. Cancer* **12**, 55–79 (2022).
56. Stone, E. et al. De novo engineering of a human cystathionine-gamma-lyase for systemic L-methionine depletion cancer therapy. *ACS Chem. Biol.* **7**, 1822–1829 (2012).
57. Gheller, B. J. et al. Extracellular serine and glycine are required for mouse and human skeletal muscle stem and progenitor cell function. *Mol. Metab.* **43**, 101106 (2021).
58. Tajan, M. et al. Serine synthesis pathway inhibition cooperates with dietary serine and glycine limitation for cancer therapy. *Nat. Commun.* **12**, 366 (2021).
59. Burlikowska, K. et al. Comparison of metabolomic profiles of organs in mice of different strains based on SPME-LC-HRMS. *Metabolites* **10**, 255 (2020).
60. Reinfeld, B. I. et al. Cell-programmed nutrient partitioning in the tumour microenvironment. *Nature* **593**, 282–288 (2021).

Methods

Clinical stable isotope tracing protocol

The human isotope tracing study was approved by the Institutional Review Board of the University of Michigan. After obtaining informed consent, eight patients with suspected GBM were enrolled onto our clinical study, which was performed perioperatively with standard-of-care craniotomies for tumour resection. Near the start of each procedure (approximately 2–4 h before tissue resection), patients received a bolus intravenous dose of [U^{13}C]glucose (8 g) followed by a continuous intravenous infusion of [U^{13}C]glucose at a rate of 4 g h^{-1}. Arterial blood was collected into EDTA-coated vials every 30–60 min for plasma preparation and analysis until intracranial tissues of interest were isolated from each patient. After initial craniotomy and tumour exposure, stereotactic image guidance was used to identify radiographically defined enhancing tumour, non-enhancing FLAIR T2 hyperintense tumour and adjacent cortical tissues. These tissues were then resected and separated by a board-certified neurosurgeon (W.N.A.-H.), rinsed in cold PBS and immediately (typically less than 3 min after resection) flash-frozen in liquid nitrogen by the research team for further analysis. Cortex and non-enhancing tumour were obtained from all eight patients. Enhancing tumour tissue was obtained from only seven patients, because one tumour comprised entirely non-enhancing disease. Tumour content quantification in human samples (cortex, enhancing tumour, non-enhancing tumour) stained with H&E was performed by a board-certified neuropathologist (S.V.). Clinical information including Ki-67 index and IDH mutation status were abstracted from the medical record and clinical pathology report. Sample size was based on maximal enrollment rather than predetermination with statistical methods, and patients were not allocated into groups. Blinding was not performed, as the paired design comparing distinctly identifiable tumour and cortex from each participant made masking impractical during sample collection and analysis; however, the quantitative nature of the data obtained by mass spectrometry mitigated potential subjective bias in interpretation.

Patient-derived orthotopic models

All animal studies were approved by the Institutional Animal Care and Use Committee (IACUC) at the University of Michigan. Mice were housed in specific-pathogen-free conditions at a temperature of 74 °F and relative humidity between 30 and 70% on a light–dark cycle of 12 h on–12 h off with unfettered access to food and water. In experiments assessing baseline ^{13}C labelling from [U^{13}C]glucose under control or serine/glycine-restricted conditions, all mice were placed on either control diets (TestDiet Baker Amino Acid Diet 5CC7) or serine/glycine-restricted diets (TestDiet Modified Baker Amino Acid Diet 5BJX) 3 days before orthotopic tumour implantation (described below) and remained on respective diets indefinitely. Before intracranial implantation and for all other experiments, mice were fed standard chow (PicoLab Laboratory Rodent Diet 5L0D).

Studies of intracranial tumour-bearing mice used three different patient-derived models that genomically and histologically reflect typical GBMs and capture heterogeneity characteristic of the disease. These models included the patient-derived HF2303 model[16,17], as well as the GBM12 and GBM38 PDXs from the PDX National Resource at Mayo Clinic[19]. Tumour tissue was propagated subcutaneously in the flanks or brains of immunodeficient mice (B6.129S7-Rag1^{tm1Mom}/J, obtained from Jackson Laboratory or bred in-house). To introduce GFP and firefly luciferase into GBM tissue and enable their fluorescence and luminescence detection, short-term explant cultures were generated from tumours and transduced by lentiviral infection (lenti-LEGO-Ig2-fluc-IRES-GFP-VSVG or lenti-CAG-dscGFP-T2ALuc-Efs-Puro-VSVG, obtained from the University of Michigan Vector Core). After infection, cells were enriched for GFP-positive populations by fluorescence-activated cell sorting or puromycin selection and then reintroduced to mice either as subcutaneous flank tumours or intracranial tumours. To generate orthotopic GBM brain tumours in B6.129S7-Rag1^{tm1Mom}/J mice, 3×10^5 to 1×10^7 cells were implanted intracranially using a stereotactic rig or guide screws to the region of the brain calculated to be the striatum in anaesthetized mice. Tumour development was then confirmed by bioluminescence imaging as described in Supplementary Methods.

In vivo tumour studies

Sample sizes for animal experiments were determined by preliminary studies and the level of observed effect. Stratified randomization was used to achieve similar starting median tumour luminescence across groups. Blinding was not possible due to the complexity of multistep procedures: group allocation, animal treatments, animal monitoring, data collection and analyses were performed independently by separate investigators, including technicians unaware of hypotheses and without stake in outcome, minimizing bias. For all experiments, B6.129S7-Rag1tm1Mom/J mice (Jackson 002216 or bred in-house) were used, except in the long-term serine/glycine restriction experiment described in Supplementary Methods, which used C57BL/6J mice (Jackson 000664) without tumours. Mice were aged 4–12 weeks at the start of experiments. All experiments used a mix of male and female mice, except for the time-course glucose tracing experiment, which comprised only female mice and was validated using non-glucose tracers in both male and female mice. The maximum allowed tumour sizes and end points were predetermined in agreement with IACUC. For subcutaneous flank tumours, these were as follows: tumour diameter exceeds 2 cm in any single dimension; tumour ulcerates greater than half its surface area; ulceration has effusion, appears infected or has haemorrhage; tumour develops in an area that impairs normal movement or physiological behaviour. For intracranial GBM-bearing mice, humane end points were determined based on clinical observations in collaboration with veterinarians with University of Michigan's Unit for Laboratory Animal Medicine. In all experiments, we followed their numerical scoring system, assigning points for appearance, physical parameters, behaviours and body condition. When predetermined scores were reached, mice meeting these end-stage criteria were humanely euthanized. No experiments exceeded tumour sizes or end points predetermined with IACUC.

Stable isotope tracing in GBM-bearing mice

At approximately 3–6 weeks after orthotopic tumour implantation, intracranial GBM-bearing mice underwent dual catheterizations, with one catheter surgically placed into the jugular vein (for tracer administration) and a second catheter placed into the carotid artery (for plasma collection during infusion). Mice were then allowed to recover from surgery for 4–5 days. Conscious, free-moving, undisturbed mice were then delivered stable isotope tracers through the intravenous line as follows: [U^{13}C]glucose administered as a bolus dose (0.4 mg per g) followed by a continuous infusion (12 ng per g per min) for a total of 4 h; ^{15}N-amide-glutamine administered as a bolus dose (0.28 mg per g) followed by a continuous infusion (5 μg per g per min) for 6 h; $^{15}N_4$-inosine[35] administered as a bolus dose (0.8 mg) followed by a continuous infusion (0.65 μg per g per min) for 6 h; or $^{13}C_3$-serine[61] delivered continuously (6.3 μg per g per min) for 6 h.

During infusions, blood was collected periodically through the arterial line into EDTA-coated vials and used to prepare plasma. At the end of infusions, ketamine (50 mg per kg) was administered into the intravenous line to rapidly induce anaesthesia. Mice were then decapitated, and tissues were extracted on dry ice. To separate orthotopic GBM from mouse cortex, we performed microdissection aided by fluorescent light that enabled us to distinguish GFP-positive tumour from GFP-negative cortex. All tissues were then immediately (less than 3 min after anaesthesia) flash-frozen in liquid nitrogen for further analysis. In experiments measuring the spatial distribution of labelled intracranial metabolites, GBM-bearing mice were administered two intraperitoneal

injections of either saline or [U^{13}C]glucose at dosages of 2 g per kg 30 min apart. At 30 min after the second injection, mice were administered a lethal dose of isoflurane (inhalation) and then decapitated. Whole brains were rapidly collected and flash-frozen in liquid nitrogen and then cryosectioned for further analysis.

MFA

To estimate nucleotide synthesis fluxes from isotopologue time-course data, in vivo MFA methods were developed. These are described in detail in Supplementary Methods and corresponding Supplementary Tables 3–13. To estimate serine contributions in brain tumours using single-timepoint data, a steady-state method was used as described in Supplementary Methods and corresponding Supplementary Table 14.

LC–MS of human and mouse samples

Flash-frozen tissue samples were homogenized in cold (−80 °C) 80% methanol. For plasma analysis, 100% methanol at −80 °C was added to plasma samples to yield a final methanol concentration of 80%. Insoluble material was then precipitated from all samples by centrifugation at 4 °C, and supernatants containing soluble metabolites were dried by nitrogen purging or vacuum centrifugation. Dried metabolites were reconstituted in 50% methanol for LC–MS analysis. Isotope labelling was determined using an Agilent system consisting of an Infinity Lab II UPLC coupled with either a 6545 or 6230 QTOF mass spectrometer (Agilent Technologies) operated by the University of Michigan Metabolomics Core, and data were analysed with values corrected for natural isotope abundance using MassHunter Profinder 10.0. We used control samples without ^{13}C or ^{15}N labelling to ensure that labelled isotopologues from mice and patients were not from contaminating species, although it is possible that isobars present only in traced samples could still contaminate peaks. For targeted analyses of metabolite abundances, the samples were prepared as described above and then analysed using the Agilent 1290 Infinity II LC–6470 Triple Quadrupole tandem mass spectrometry system (Agilent Technologies). For compound optimization, calibration and data acquisition, Agilent MassHunter Quantitative Analysis Software v.B.08.02 was used. Retention times, transitions, buffers and gradient compositions are described in Supplementary Methods and Supplementary Table 15. For in vitro patient-derived gliomaspheres, MS and analyses of serine, glycine and phosphoglycerate are described in Supplementary Methods.

MALDI MS analysis of mouse-derived specimens

Standard microscopy slides with mounted tissue were vacuum desiccated for 20 min before matrix coating. After desiccation, the slides were sprayed with NEDC matrix (10 mg ml^{-1}, 1:1 ACN:H_2O) using an M3+ sprayer (HTX Technologies; flow rate, 75 µl min^{-1}; temperature, 70 °C; velocity, 1,000 mm min^{-1}; track spacing, 1 mm; pattern, crisscross; drying time, 0 s). The slides were mounted into a MTP Slide Adapter II (Bruker Daltonics) before analysis.

MALDI imaging data were acquired using the timsTOF fleX MALDI-2 mass spectrometer (Bruker Daltonics) operating in transmission mode with a 20 µm raster size, acquiring m/z 100–600. The laser (Bruker Daltonics; SmartBeam 3D, 355 nm, 5,000 Hz repetition rate) used a 16 µm beam scan, resulting in a 20 µm × 20 µm ablation area. Taurine was used as a lock mass ([M-H]1-, m/z 124.0074).

MS imaging data were visualized using SCiLS Lab 2023b, with single fractional enrichment, normalized mean enrichment and fractionalized enrichment images generated in SCiLS Lab using an in-house script using the SCiLS REST API (Bruker Daltonics; v.6.2.114), written in R (v.4.2.2), using RStudio (2022.12.0 build 353). A segmentation algorithm built into SCiLS Lab was used to create four data-driven regions corresponding to the healthy and GBM tissue in the ^{13}C dosed and control tissues (normalization, total ion count; denoising, weak; method, bisecting k-means; metric, Manhattan). The relative isotopologue intensity of these regions was also calculated with another in-house script implemented through the SCiLS REST API.

Tentative annotations were performed using MetaboScape 2023 (Bruker Daltonics) using target lists of known biological molecules generated with the TASQ 2022 software (Bruker Daltonics; amino acids, glycolysis, citrate cycle). The molecular formula of target molecules was used to calculate an accurate mass for each target. Annotations required a mass error of less than 3.0 ppm. In total, 72 features were annotated using this limited list, with annotated peaks having a mass accuracy of 1.1 ppm.

Spatial metabolite imaging and analysis of human clinical specimens are detailed in Supplementary Methods.

Chemoradiation treatments and tumour burden studies

In experiments evaluating the influence of RT on metabolism, cannulated mice were anaesthetized by 2% isoflurane inhalation and then treated with cranially directed RT at a dose of 8 Gy or sham RT with a lead shield keeping the cranium exposed. Immediately after RT (less than 5 min), the mice were removed from anaesthesia and administered tracer infusions as described above.

In studies assessing animal survival, mice were placed onto either a control diet (TestDiet Baker Amino Acid Diet, 5CC7) or a modified diet containing 0% serine and 0% glycine with all other amino acids adjusted to account for serine and glycine reduction (TestDiet Modified Baker Amino Acid Diet, 5BJX) 3 days before orthotopic tumour implantation. The mice were then implanted with luciferase-positive intracranial tumours and maintained on respective diets for the remainder of experimentation. Once bioluminescence imaging (described in the Supplementary Methods) detected intracranial tumours with flux values of 10^6–10^7 p s^{-1} (9 to 50 days after implantation), the mice on each diet were randomized into control or chemoradiation-treated groups. On each treatment day, mice received both TMZ (oral administration) and cranial RT (under isoflurane anaesthesia with a lead shield keeping cranium exposed), with RT administered 1 h after TMZ treatment. GBM12-bearing mice were administered chemoradiation as three consecutive days of TMZ (25 mg per kg) and cranial RT (2 Gy). GBM38-bearing mice were administered chemoradiation as 3 consecutive days of TMZ (50 mg per kg) and cranial RT (2 Gy). HF2303-bearing mice were administered chemoradiation in two cycles, with 13 days between cycles. The first cycle consisted of 4 consecutive daily doses of TMZ (25 mg per kg) and RT (2 Gy). The second cycle consisted of 2 consecutive treatment days, a 2 day gap, and then 1 treatment day. A schematic of the treatment schemes is provided in Extended Data Fig. 11j–l. Overall survival was determined using the Kaplan–Meier method, with log-rank tests used to compare survival curves.

Histological analyses were performed as previously described[7] by H&E staining and Ki-67 staining. The primary antibody for Ki-67 (BD Biosciences, 550609) was used at a 1:1,000 dilution. Immunohistochemical staining was performed using the Vectastain Elite ABC Kit (PK-6102), which included the secondary antibody (1:200). Further details and quantification are described in Supplementary Methods.

Analysis of metabolite enrichment

To quantify the incorporation of stable isotope tracers into metabolites, we calculated mean enrichment, defined as the average percentage of labelled atoms (^{13}C or ^{15}N) within a metabolite pool[62], corrected for natural abundance:

$$\text{Mean enrichment} = \frac{\sum_{i=0}^{n} i \times m_i}{n \times \sum_{i=0}^{n} m_i}$$

where n is the number of C or N atoms in the metabolite, i represents isotopologues and m represents isotopologue abundance. This metric captures the total fractional contribution of tracers to metabolites of interest, averaging labelling across all isotopologues. Alternatively,

specific isotopologue fractions or relative abundance were used to track specific metabolic pathways. When appropriate and where indicated, tissue enrichment values were normalized to plasma tracer enrichment. Detailed analysis methods are described in the figure legends. Isotopologues and mean enrichment percentages were determined using MassHunter Profinder v.10.0 (Agilent Technologies).

Descriptive statistics (mean, s.d.) for metabolite enrichments are graphically presented. Comparisons between groups were performed using linear models for unpaired data and linear mixed-effects models for paired (for example, cortex and tumour from the same individual) or repeated-measures data (for example, in cases of multiple tumour foci extracted from a single mouse). Holm's method was used to adjust for multiple comparisons performed for each metabolite. All tests were two-sided, and statistical significance was assessed at the 0.05 significance level. Statistical comparisons and parameters are further described in the figure legends. Analyses were performed using R v.4.4.2 or GraphPad Prism 10.

Additional experimental information

No commonly misidentified cell lines were used in this study. The GBM374gs gliomasphere model was authenticated regularly via short tandem repeat fingerprinting using the GenePrint 10 system (Laragen). All experiments involving GBM12, GBM38 and HF2303 patient-derived models were performed in vivo, with the exception of in vitro culturing for lentiviral GFP and luciferase transduction, and were not authenticated beyond primary isolation; in vivo passage and marker retention ensured identity of these models. All models cultured in vitro were tested regularly for mycoplasma using the MycoAlert Mycoplasma Detection Kit (Lonza) and confirmed negative. Comprehensive experimental and analytical details including metabolite imaging of clinical samples, LC–MS, subtype and transcriptional analyses of our data and others[63–65], development of MFA methods, in vitro gliomasphere experiments, additional in vivo methods, and histological staining and quantification protocols are found in Supplementary Methods, containing refs. 66–99.

Statistics and reproducibility

Human data were obtained from the same cohort of patients throughout the study. Labelled human samples were analysed from eight patients, comprising $n = 8$ cortex samples, $n = 7$ enhancing tumour samples, and $n = 8$ non-enhancing tumour samples. One patient lacked enhancing tumour tissue. Mouse LC–MS data corresponding to [$U^{13}C$]glucose labelling and metabolite abundance in HF2303 and GBM12 models were from the same cohorts throughout the study. Mouse LC–MS data corresponding to single-timepoint [$U^{13}C$]glucose labelling in GBM38-bearing mice were from the same cohort throughout the study. For all mouse LC–MS data showing single-timepoint labelling from [$U^{13}C$]glucose, samples were analysed from sixteen total mice with $n = 16$ cortex samples and comprised: seven GBM38-bearing mice with $n = 7$ tumour foci and $n = 7$ cortex samples; five GBM12-bearing mice with $n = 5$ tumour foci and $n = 5$ cortex samples; and four HF2303-bearing mice with five tumour foci, one of which was diffuse and cortically contaminated and was therefore excluded from analysis, yielding $n = 4$ tumour foci and $n = 4$ cortex samples. One of these HF2303-bearing mice exhibited suboptimal data quality for plasma glucose measurements used to normalize tissue labelling. Therefore, plasma glucose enrichment for this mouse was estimated using the mean value derived from remaining mice in the group. Mouse data corresponding to single-timepoint metabolite abundance in GBM38-bearing mice were from the same cohort throughout the study. All time course [$U^{13}C$]glucose labelling data were from the same cohort of mice. All data showing in vivo isotope labelling from ^{15}N-glutamine were from the same cohort of mice. All data showing in vivo isotope labelling from $^{15}N_4$-inosine were from the same cohort of mice. Mouse tissue spatial imaging data and matched H&E staining shown throughout this study are from the same ^{13}C-labelled and negative control unlabelled mice. In developing our hypothesis-generating metabolic flux models of nucleotide synthesis, the need for multiple timepoints constrained sample numbers at each timepoint, and exclusions were necessary to minimize variance within groups and ensure data robustness. Specific exclusion criteria are described at https://github.com/baharm1/iMFA/, and model-based predictions were validated by multiple orthogonal tracers. Mice failing to form intracranial tumours post-orthotopic implantation (<5%) or dying 0–5 days after implantation (<5%) or jugular/carotid catheter placement (<10%), likely due to surgical complications, were excluded. In LC–MS experiments, metabolites below detection thresholds were excluded.

Stable isotope infusion studies in human patients inherently lack full repeatability because of substantial variability among individuals, clinical-protocol-related factors and restricted tissue quantities. Labelled glucose infusion studies of intracranial GBM38-bearing mice were performed three or more times. In vivo glucose labelling studies were further repeated by five or more serial labelled glucose injection experiments using intracranial HF2303 tumour-bearing mice, intracranial GBM38 tumour-bearing mice, and two additional intracranial models not presented. In vivo serine tracer uptake measurements were replicated via serial tracer injection into intracranial GBM38-bearing mice. Studies with amide-labelled glutamine infusions showed consistent GBM versus cortex label patterns in three or more independent experiments. In vitro gliomasphere experiments were performed three times. All attempts at replicating the experiments were successful.

For Fig. 1d, the numbers of mice analysed at each timepoint are as follows: $n = 10$ at 0 min, $n = 7$ at 5 min, $n = 10$ at 30 min, $n = 10$ at 30 min, $n = 5$ at 45 min, $n = 8$ at 60 min, $n = 5$ at 120 min, $n = 3$ at 180 min and $n = 3$ at 240 min. For Fig. 1e, samples were analysed from eight patients, comprising $n = 8$ cortex samples, $n = 7$ enhancing tumour samples and $n = 8$ non-enhancing tumour samples. Some metabolites were not reliably detected in every tissue sample and were not shown. Therefore, sample numbers corresponding to each metabolite are as follows: GAP/DHAP: cortex, $n = 8$; enhancing, $n = 6$; non-enhancing, $n = 8$. 3PG/2PG: cortex, $n = 7$; enhancing, $n = 7$; non-enhancing, $n = 6$. PEP: cortex, $n = 5$; enhancing, $n = 6$; non-enhancing, $n = 5$. Pyruvate: cortex, $n = 8$; enhancing, $n = 7$; non-enhancing, $n = 7$. Lactate: cortex, $n = 8$; enhancing, $n = 7$; non-enhancing, $n = 8$. For Fig. 1f, samples were analysed from 16 total mice with $n = 16$ cortex samples and comprised 7 GBM38-bearing mice with $n = 7$ tumour foci and $n = 7$ cortex samples; five GBM12-bearing mice with $n = 5$ tumour foci and $n = 5$ cortex samples; and four HF2303-bearing mice with five tumour foci, one of which was diffuse and cortically contaminated and was therefore excluded from analysis, yielding $n = 4$ tumour foci and $n = 4$ cortex samples. Some metabolites were not reliably detected in every tissue sample and were not shown. Therefore, the sample numbers corresponding to each metabolite are as follows: FBP: cortex, $n = 16$; HF2303, $n = 4$; GBM12, $n = 5$; GBM38, $n = 7$. GAP/DHAP: cortex, $n = 15$; HF2303, $n = 3$; GBM12, $n = 4$; GBM38, $n = 6$. 3PG/2PG: cortex, $n = 6$; HF2303, $n = 4$; GBM12, $n = 4$; GBM38, $n = 6$. Pyruvate: cortex, $n = 15$; HF2303, $n = 4$; GBM12, $n = 5$; GBM38, $n = 7$. Lactate: cortex, $n = 16$; HF2303, $n = 4$; GBM12, $n = 5$; GBM38, $n = 7$.

For Fig. 2a,c,g,j,l, samples were analysed from eight patients, comprising $n = 8$ cortex samples, $n = 7$ enhancing tumour samples and $n = 8$ non-enhancing tumour samples. Some metabolites were not reliably detected in every tissue sample and were not shown. Therefore, sample numbers corresponding to each metabolite are as follows. Figure 2a: citrate/isocitrate, α-ketoglutarate and malate: cortex, $n = 8$; enhancing, $n = 7$; non-enhancing, $n = 8$. Succinate: cortex, $n = 7$; enhancing, $n = 6$; non-enhancing, $n = 8$. Figure 2c: glutamate and glutamine: cortex, $n = 8$; enhancing, $n = 7$; non-enhancing, $n = 8$. GABA: cortex, $n = 5$; enhancing, $n = 5$; non-enhancing, $n = 4$. Aspartate: cortex, $n = 6$; enhancing, $n = 5$; non-enhancing, $n = 6$. Figure 2g: IMP: cortex, $n = 8$; enhancing, $n = 6$; non-enhancing, $n = 8$. Inosine, GMP, guanosine, AMP and ADP:

cortex, $n = 8$; enhancing, $n = 7$; non-enhancing, $n = 8$. GDP: cortex, $n = 7$; enhancing, $n = 6$; non-enhancing, $n = 7$. Figure 2j: UMP: cortex, $n = 8$; enhancing, $n = 6$; non-enhancing, $n = 8$; dTDP: cortex, $n = 8$; enhancing, $n = 4$; non-enhancing, $n = 8$. Figure 2l: NAD: cortex, $n = 8$; enhancing, $n = 7$; non-enhancing, $n = 7$. NADH: cortex, $n = 8$; enhancing, $n = 7$; non-enhancing, $n = 5$. Samples in Fig. 2b,d,h,k,m were analysed from 16 total mice with $n = 16$ cortex samples and comprised 7 GBM38-bearing mice with $n = 7$ tumour foci and $n = 7$ cortex samples; five GBM12-bearing mice with $n = 5$ tumour foci and $n = 5$ cortex samples; and four HF2303-bearing mice with five tumour foci, one of which was diffuse and cortically contaminated and was therefore excluded from analysis, yielding $n = 4$ tumour foci and $n = 4$ cortex samples. Some metabolites were not reliably detected in every tissue sample and were not shown. Therefore, sample numbers corresponding to each metabolite are as follows. Figure 2b: for all metabolites: cortex, $n = 16$; HF2303, $n = 4$; GBM12, $n = 5$; GBM38, $n = 7$. Figure 2d: glutamate and aspartate: cortex, $n = 16$; HF2303, $n = 4$; GBM12, $n = 5$; GBM38, $n = 7$. Glutamine: cortex, $n = 16$; HF2303, $n = 4$; GBM12, $n = 5$; GBM38, $n = 3$. GABA: cortex, $n = 12$; HF2303, $n = 3$; GBM38, $n = 6$. Figure 2h: IMP: cortex, $n = 16$; HF2303, $n = 4$; GBM12, $n = 5$; GBM38, $n = 6$. GMP, GDP, AMP, ADP and ATP: cortex, $n = 16$; HF2303, $n = 4$; GBM12, $n = 5$; GBM38, $n = 7$. GTP: cortex, $n = 12$; GBM12, $n = 5$; GBM38, $n = 7$. Figure 2k: UMP: cortex, $n = 16$; HF2303, $n = 4$; GBM12, $n = 5$; GBM38, $n = 7$; CMP: cortex, $n = 12$; GBM12, $n = 5$; GBM38, $n = 7$. dTDP: cortex, $n = 13$; HF2303, $n = 4$; GBM12, $n = 5$. Figure 2m, NAD: cortex, $n = 16$; HF2303, $n = 4$; GBM12, $n = 5$; GBM38, $n = 7$; NADH: cortex, $n = 15$; HF2303, $n = 4$; GBM12, $n = 5$; GBM38, $n = 7$.

n values for Fig. 3 are shown in the figure caption. For Fig. 4a, samples were analysed from eight patients, comprising $n = 8$ cortex samples, $n = 7$ enhancing tumour samples and $n = 8$ non-enhancing tumour samples. For Fig. 4b, samples were analysed from 16 total mice with $n = 16$ cortex samples and comprised 7 GBM38-bearing mice with $n = 7$ tumour foci and $n = 7$ cortex samples, 5 GBM12-bearing mice with $n = 5$ tumour foci and $n = 5$ cortex samples, and 4 HF2303-bearing mice with 5 tumour foci, one of which was diffuse and cortically contaminated and was therefore excluded from analysis, yielding $n = 4$ tumour foci and $n = 4$ cortex samples. For Fig. 4d, samples were analysed from 5 GBM-bearing mice, comprising $n = 5$ cortex samples and $n = 5$ tumour samples. For Fig. 4e, samples were analysed from 5 GBM-bearing mice, comprising $n = 4$ cortex samples and $n = 4$ tumour samples. For Fig. 4f, samples were analysed from five GBM-bearing mice, comprising $n = 5$ cortex samples and $n = 5$ tumour samples. For Fig. 4i, animal numbers are as follows: control diet, $n = 7$; −SG diet, $n = 8$; control diet with chemoradiation, $n = 8$; −SG diet with chemoradiation, $n = 9$. For Fig. 4j, animals were examined over three independent experiments with total mouse numbers as follows: control diet, $n = 14$; −SG diet, $n = 14$; control diet with chemoradiation, $n = 11$; −SG diet with chemoradiation, $n = 9$. In one of these experiments, three mice were excluded due to lack of detectable brain tumour and one mouse was excluded due to an unrelated condition requiring its humane euthanasia. For Fig. 4k, animals were examined over two independent experiments with total mouse numbers as follows: control diet, $n = 18$; −SG diet, $n = 21$; control diet with chemoradiation, $n = 10$; −SG diet with chemoradiation, $n = 13$. For Fig. 4m, data corresponding to control diets are from the same HF2303-bearing mice described in Fig. 4b. Moreover, data corresponding to −SG diets were obtained from four HF2303-bearing mice with four cortex samples and four tumour samples. Thus, sample numbers are as follows: for control diet, $n = 4$ cortex samples and $n = 4$ tumour samples; and, for the −SG diet, $n = 4$ cortex samples and $n = 4$ tumour samples. For Fig. 4n, data are from the same mice as described in Fig. 4b,m. These samples comprised $n = 4$ control tumour samples and $n = 4$ −SG tumour samples.

Reporting summary

Further information on research design is available in the Nature Portfolio Reporting Summary linked to this article.

Data availability

RNA-seq data generated in this study are accessible through GEO series accession number GSE299102. The TCGA-GBM dataset[63] used in this study was accessed from GDC portal (13 December 2024). The two RNA-seq datasets[64,65] used in this study are available at the GEO under accession numbers GSE59612 and GSE165595. All other data supporting the findings of this study are available within the Article and its Supplementary Information. Source data are provided with this paper.

Code availability

Codes generated in this study were deposited at GitHub (https://github.com/baharm1/iMFA/).

61. Li, X. et al. Circulating metabolite homeostasis achieved through mass action. *Nat. Metab.* **4**, 141–152 (2022).
62. Buescher, J. M. et al. A roadmap for interpreting ^{13}C metabolite labeling patterns from cells. *Curr. Opin. Biotechnol.* **34**, 189–201 (2015).
63. Wang, Q. et al. Tumor evolution of glioma-intrinsic gene expression subtypes associates with immunological changes in the microenvironment. *Cancer Cell* **32**, 42–56 (2017).
64. Hwang, T. et al. Genome-wide perturbations of Alu expression and Alu-associated post-transcriptional regulations distinguish oligodendroglioma from other gliomas. *Commun. Biol.* **5**, 62 (2022).
65. Gill, B. J. et al. MRI-localized biopsies reveal subtype-specific differences in molecular and cellular composition at the margins of glioblastoma. *Proc. Natl Acad. Sci. USA* **111**, 12550–12555 (2014).
66. Rafols, P. et al. rMSIproc: an R package for mass spectrometry imaging data processing. *Bioinformatics* **36**, 3618–3619 (2020).
67. Loos, M., Gerber, C., Corona, F., Hollender, J. & Singer, H. Accelerated isotope fine structure calculation using pruned transition trees. *Anal. Chem.* **87**, 5738–5744 (2015).
68. Fernandez, C. A., Des Rosiers, C., Previs, S. F., David, F. & Brunengraber, H. Correction of 13C mass isotopomer distributions for natural stable isotope abundance. *J. Mass Spectrom.* **31**, 255–262 (1996).
69. Young, J. D., Walther, J. L., Antoniewicz, M. R., Yoo, H. & Stephanopoulos, G. An elementary metabolite unit (EMU) based method of isotopically nonstationary flux analysis. *Biotechnol. Bioeng.* **99**, 686–699 (2008).
70. Antoniewicz, M. R. A guide to ^{13}C metabolic flux analysis for the cancer biologist. *Exp. Mol. Med.* **50**, 1–13 (2018).
71. Byrd, R. H., Nocedal, J. & Waltz, R. A. in *Large-Scale Nonlinear Optimization. Nonconvex Optimization and Its Applications* (Di Pillo, G. & Roma, M. (eds)) Vol. 83, 35–59 (Springer, 2006).
72. Antoniewicz, M. R., Kelleher, J. K. & Stephanopoulos, G. Determination of confidence intervals of metabolic fluxes estimated from stable isotope measurements. *Metab. Eng.* **8**, 324–337 (2006).
73. Quek, L. E. et al. Dynamic ^{13}C flux analysis captures the reorganization of adipocyte glucose metabolism in response to insulin. *iScience* **23**, 100855 (2020).
74. Kreutz, C., Raue, A. & Timmer, J. Likelihood based observability analysis and confidence intervals for predictions of dynamic models. *BMC Syst. Biol.* **6**, 120 (2012).
75. Kanehisa, M. & Goto, S. KEGG: Kyoto Encyclopedia of Genes and Genomes. *Nucleic Acids Res.* **28**, 27–30 (2000).
76. Sjostedt, E. et al. An atlas of the protein-coding genes in the human, pig, and mouse brain. *Science* **367**, eaay5947 (2020).
77. Cai, F. et al. Comprehensive isotopomer analysis of glutamate and aspartate in small tissue samples. *Cell Metab.* **35**, 1830–1843 (2023).
78. Jinnah, H. A., Page, T. & Friedmann, T. Brain purines in a genetic mouse model of Lesch-Nyhan disease. *J. Neurochem.* **60**, 2036–2045 (1993).
79. Burdett, T. C. et al. Efficient determination of purine metabolites in brain tissue and serum by high-performance liquid chromatography with electrochemical and UV detection. *Biomed. Chromatogr.* **27**, 122–129 (2013).
80. Cruz, T. et al. Identification of altered brain metabolites associated with TNAP activity in a mouse model of hypophosphatasia using untargeted NMR-based metabolomics analysis. *J. Neurochem.* **140**, 919–940 (2017).
81. Zheng, H. et al. The hypothalamus as the primary brain region of metabolic abnormalities in APP/PS1 transgenic mouse model of Alzheimer's disease. *Biochim. Biophys. Acta* **1864**, 263–273 (2018).
82. Lu, Z. et al. Quantitative analysis of 20 purine and pyrimidine metabolites by HILIC-MS/MS in the serum and hippocampus of depressed mice. *J. Pharm. Biomed. Anal.* **219**, 114886 (2022).
83. Tanaka, K. et al. Glioma cells require one-carbon metabolism to survive glutamine starvation. *Acta Neuropathol. Commun.* **9**, 16 (2021).
84. Shank, R. P. & Aprison, M. H. The metabolism in vivo of glycine and serine in eight areas of the rat central nervous system. *J. Neurochem.* **17**, 1461–1475 (1970).
85. Jang, C. et al. Metabolite exchange between mammalian organs quantified in pigs. *Cell Metab.* **30**, 594–606 (2019).
86. Schmidt, K., Carlsen, M., Nielsen, J. & Villadsen, J. Modeling isotopomer distributions in biochemical networks using isotopomer mapping matrices. *Biotechnol. Bioeng.* **55**, 831–840 (1997).
87. Shipley, R. A. & Clark, R. E. Tracer *Methods for in vivo Kinetics: Theory and Applications* (Academic, 1972).
88. Brennan, C. W. et al. The somatic genomic landscape of glioblastoma. *Cell* **155**, 462–477 (2013).

89. Reich, M. et al. GenePattern 2.0. *Nat. Genet.* **38**, 500–501 (2006).
90. Subramanian, A. et al. Gene set enrichment analysis: a knowledge-based approach for interpreting genome-wide expression profiles. *Proc. Natl Acad. Sci. USA* **102**, 15545–15550 (2005).
91. Bowman, R. L., Wang, Q., Carro, A., Verhaak, R. G. & Squatrito, M. GlioVis data portal for visualization and analysis of brain tumor expression datasets. *Neuro Oncol.* **19**, 139–141 (2017).
92. Aibar, S. et al. SCENIC: single-cell regulatory network inference and clustering. *Nat. Methods* **14**, 1083–1086 (2017).
93. Rouillard, A. D. et al. The harmonizome: a collection of processed datasets gathered to serve and mine knowledge about genes and proteins. *Database* **2016**, baw100 (2016).
94. Diamant, I., Clarke, D. J. B., Evangelista, J. E., Lingam, N. & Ma'ayan, A. Harmonizome 3.0: integrated knowledge about genes and proteins from diverse multi-omics resources. *Nucleic Acids Res.* **53**, D1016–D1028 (2025).
95. Barrett, T. et al. NCBI GEO: archive for functional genomics data sets–update. *Nucleic Acids Res.* **41**, D991–D995 (2013).
96. Kerk, S. A. et al. Metabolic requirement for GOT2 in pancreatic cancer depends on environmental context. *eLife* **11**, e73245 (2022).
97. Park, J. O. et al. Near-equilibrium glycolysis supports metabolic homeostasis and energy yield. *Nat. Chem. Biol.* **15**, 1001–1008 (2019).
98. Wang, Y., Parsons, L. R. & Su, X. AccuCor2: isotope natural abundance correction for dual-isotope tracer experiments. *Lab. Invest.* **101**, 1403–1410 (2021).
99. Su, X., Lu, W. & Rabinowitz, J. D. Metabolite spectral accuracy on orbitraps. *Anal. Chem.* **89**, 5940–5948 (2017).

Acknowledgements We thank the patients enrolled in our clinical tracing study, whose courage and generosity made key discoveries possible; the members of the neurosurgical team at the University of Michigan for assisting with human stable isotope infusions; R. DeBerardinis for his advice and expertise in human stable isotope tracing; G. Hoxhaj for sharing protocols for in vivo isotopic inosine infusions; A. Rehemtulla, A. deCarvalho and the members of the Henry Ford Health System for sharing the patient-derived HF2303 model; H. Kornblum for sharing the patient-derived GBM374gs gliomasphere model; H. Baum, T. Rajendiran, A. Wiggins, C. Evans and A. Elaimy for technical support; and C. Cheng for providing advice on editorial revisions to the manuscript. Animal management, technical and experimental support services were provided by the University of Michigan Unit for Laboratory Animal Medicine (ULAM), the University of Michigan Metabolomics Core (University of Michigan Medical School, Biomedical Research Core Facilities), the University of Michigan Vector Core (University of Michigan Medical School, Biomedical Research Core Facilities), the ULAM Pathology Core, and the Center for Molecular Imaging at the University of Michigan. A.J.S. was supported by the NCI (K99CA300923 and F32CA260735); P. Sravya by the American Cancer Society Postdoctoral Fellowship (PF-23-1077428-01-MM, https://doi.org/10.53354/ACS.PF-23-1077428-01-MM.pc.gr.175459); E.V. and J.B. by the NCI (CA251872 and CA251872-S1); J.B. by a UCLA JCCC Fellowship Award; J.O.P. by the NIGMS (R35GM143127); Z.W., J.F. and N.Q. by the NIDDK MMPC-Live (1U2CDK135066); and W.Z. by the University of Michigan Medical School Pandemic Research Recovery grant (U083054). Funding for J.N.S. was provided by Mayo Clinic and the William H. Donner Professorship. S.V. was supported by the NINDS (R01NS110572 and R01NS127799) and the NCI (R01CA261926). Funding for N.Y.R.A. was provided by the Daniel E. Ponton Fund, the National Brain Tumour Society, the Mass Life Sciences Center and the NCI (U54CA283114). W.N.A.-H. was supported by the NINDS (K08NS12827101), the American Cancer Society (CSDG-23-1031584-01-MM) and the American Brain Tumour Association; D.N. by the NCI (R01CA271369); D.R.W. by the NCI (K08CA234416 and R37CA258346), the NINDS (R01NS129123), the Damon Runyon Cancer Foundation, the Sontag Foundation, the Ivy Glioblastoma Foundation, the Forbes Institute for Cancer Discovery, Alex's Lemonade Stand Foundation and the Chad Tough Defeat DIPG foundation; and D.R.W. and T.S.L. by the NCI (P50CA269022).

Author contributions A.J.S., A.M., B.M., C.A.L., W.N.A.-H., D.N. and D.R.W. conceived the study and designed the experiments. A.J.S., A.M., B.M., E.V., C.A.L., W.N.A.-H., D.N. and D.R.W. wrote and revised the manuscript. C.A.L., W.N.A.-H., D.N. and D.R.W. supervised the project. D.N., A.M., B.M. and A.A. designed and performed the metabolic flux analyses and bioinformatic analyses. D.R.W. wrote the clinical study and enrolled patients. A.J.S., D.R.W., A.U.K., A.O., K.A.R. and V.T. performed the patient glucose infusions and collection of patient plasma and tissues. W.N.A.-H. performed the patient tumour resections. A.J.S., A.O., K.W.-R., N.R.Q. and D.R.W. managed the animal studies. A.J.S., A.O., K.W.-R. and A.U.K. performed the orthotopic tumour implantations, chemoradiation administration and intracranial tumour-monitoring luminescence and survival studies. A.J.S., A.O., Z.W., J.F. and N.R.Q. performed the mouse isotope infusions and sample collection. S.S. provided support for animal studies. C.A.L. supervised and analysed LC–MS experiments of human and mouse samples. A.J.S., A.O., A.U.K., L.Z., P. Sajjakulnukit and A.C.A. performed extraction, processing, and LC–MS of human and mouse metabolites. A.J.S., N.L., P. Sravya, L.Z. and P. Sajjakulnukit analysed human and mouse LC–MS data. B.M., D.M.E., W.N.A.-H. and D.R.W. analysed patient transcriptional and clinical data. W.Z., J.X., A.L., N.K., A.O. and K.W.-R. performed tissue collection, histological staining and stain analyses of intracranial tissues from GBM-bearing mice for tumour burden studies. J.B., J.O.P., J.t.H. and E.V. performed, supervised and analysed the in vitro gliomasphere serine restriction studies. J.L.F. and E.Y. performed MS imaging, tissue-matched H&E and analysis of mouse samples. M.S.R., S.A.S., G.B. and N.Y.R.A. performed MS imaging, tissue-matched H&E and analysis of human samples. A.J.S. and A.O. performed and analysed animal growth and haematological experiments. K.S. provided statistical support. J.N.S. provided mouse brain tumour models and advice regarding their use. S.V. performed the tumour content analysis of clinical samples. T.S.L. provided guidance on writing and overall study design and interpretation. D.R.W., D.N., W.N.A.-H. and C.A.L. provided resources and funding.

Competing interests D.R.W. has consulted for Agios Pharmaceuticals, Admare Pharmaceuticals, Bruker and Innocrin Pharmaceuticals. D.R.W. is listed as an inventor on patents pertaining to the treatment of patients with brain tumours (US provisional patent application 63/416,146, US provisional patent application 62/744,342, US provisional patent application 62/724,337). A.J.S., D.N., C.A.L., A.M., A.A. and B.M. are listed as co-inventors on US provisional patent application 63/416,146. N.Y.R.A. reports the following disclosures: key opinion leader to Bruker Daltonics, collaboration with Thermo Finnigan, service agreement with EMD Serono, service agreement with iTeos Therapeutics, and founder and board member of BondZ. In the past three years, C.A.L. has consulted for Odyssey Therapeutics and Third Rock Ventures. W.N.A.-H. has consulted for Servier Pharmaceuticals. The other authors declare no competing interests.

Additional information

Supplementary information The online version contains supplementary material available at https://doi.org/10.1038/s41586-025-09460-7.

Correspondence and requests for materials should be addressed to Costas A. Lyssiotis, Wajd N. Al-Holou, Deepak Nagrath or Daniel R. Wahl.

Peer review information *Nature* thanks Sheila Singh and the other, anonymous, reviewer(s) for their contribution to the peer review of this work.

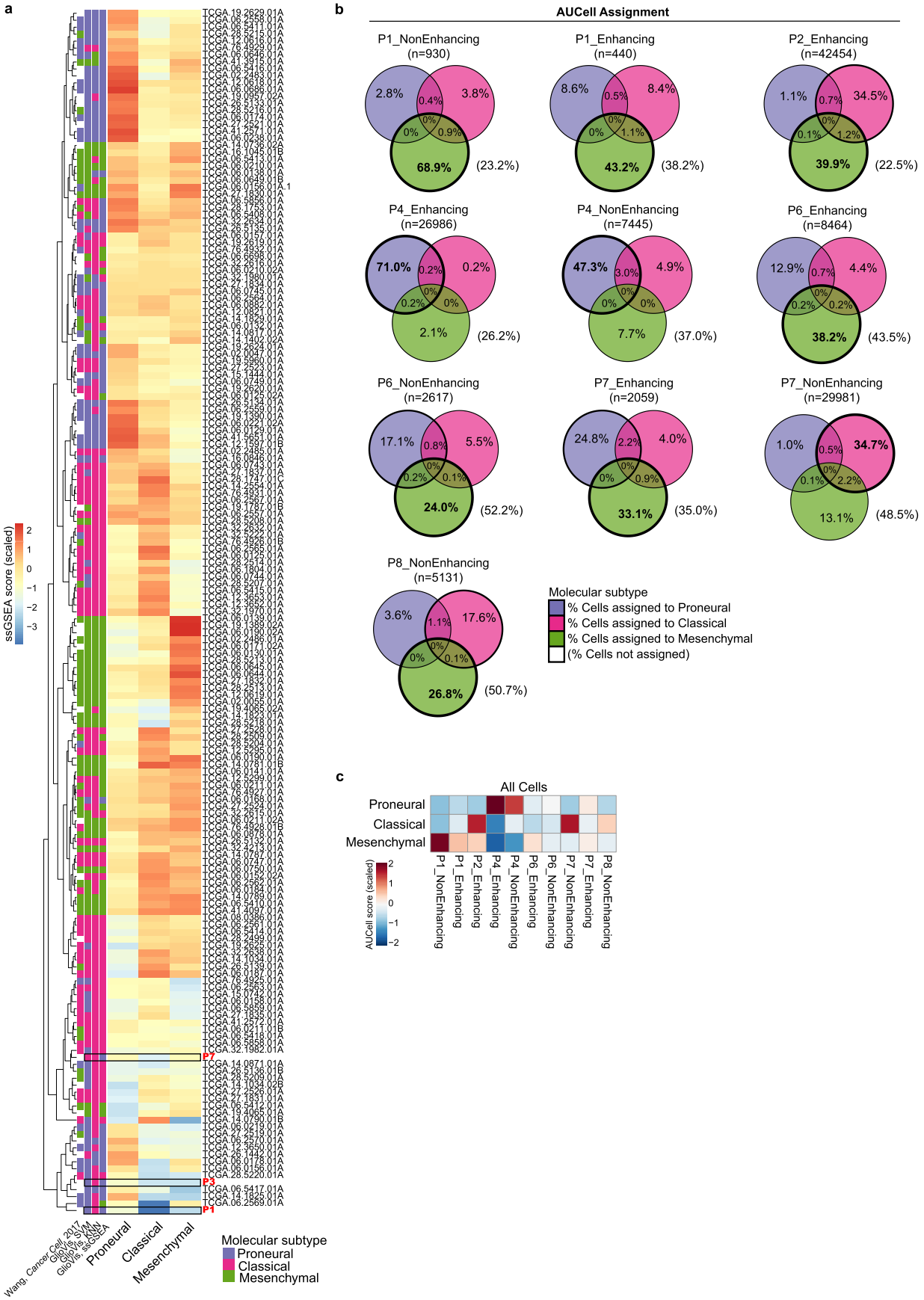

Extended Data Fig. 1 | See next page for caption.

Extended Data Fig. 1 | Transcriptional profiling of human brain tumours. **a**, Heatmap of single sample gene set enrichment analysis (ssGSEA) scores using 150 signature genes of proneural, classical, and mesenchymal subtypes for 170 GBM samples of TCGA and three patients from this study based on the availability of bulk RNA-seq data. Samples were grouped by hierarchical clustering. Four methods were used to identify molecular subtypes: hierarchical clustering, support vector machine (SVM), k-nearest neighbour (KNN), ssGSEA. The latter three methods were used on GlioVis portal. Subtypes of TCGA samples have been predicted in Wang et al.[63] and were used to assess GlioVis methods. **b**, Venn diagrams of percentages of cells assigned to each molecular subtype based on AUCell scores using scRNA-seq data. n represents the number of cells passed quality control for each patient tissue. **c**, Heatmap of AUCell score of 150 signature genes for molecular subtypes using scRNA-seq data. Abbreviations: ssGSEA (single sample gene set enrichment analysis), SVM (support vector machine), KNN (k-nearest neighbour).

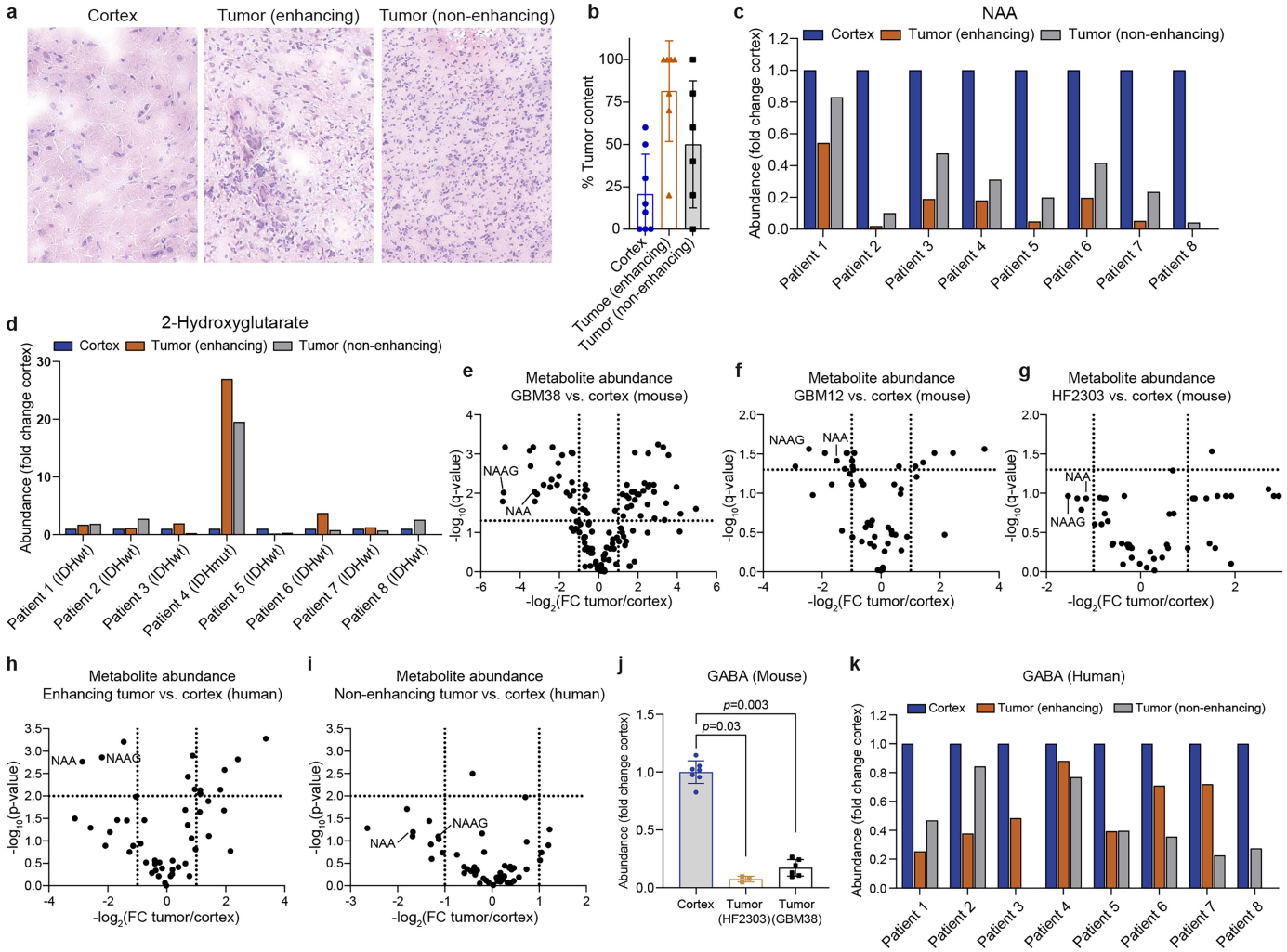

Extended Data Fig. 2 | Histological and metabolic validation of tumour and cortex sample separation. a, Representative H&E stains of tissues resected from our cohort of 8 glioma patients. **b**, Percent tumour content in tissues from each patient was defined by a clinical neuropathologist (SV). Data are mean ± s.d. **c**, Levels of NAA in cortical tissue and tumour tissue (enhancing and non-enhancing) from human glioma patients undergoing surgical resection. **d**, Levels of 2-hydroxyglutarate in cortical tissue and tumour tissue (enhancing and non-enhancing) from human glioma patients undergoing surgical resection. **e-i**, Volcano plots of metabolite abundance determined by LC-MS were used to assess fold change in tumour metabolite levels compared to cortical metabolite levels as follows: **e**, GBM compared to cortex in orthotopic GBM38-bearing mice, **f**, GBM compared to cortex in orthotopic GBM12-bearing mice, and **g**, GBM compared to cortex in orthotopic HF2303-bearing mice, **h**, enhancing tumour compared to cortex in patients, and **i**, non-enhancing tumour compared to cortex in patients. **j**, Levels of GABA in intracranial tissues from orthotopic GBM-bearing mice. Data are mean ± s.d. **k**, Levels of GABA in cortical tissue and tumour tissue (enhancing and non-enhancing) from human glioma patients undergoing surgical resection. Abbreviations: NAA (N-acetylaspartate), NAAG (N-acetylaspartylglutamate), GABA (gamma-aminobutyric acid).

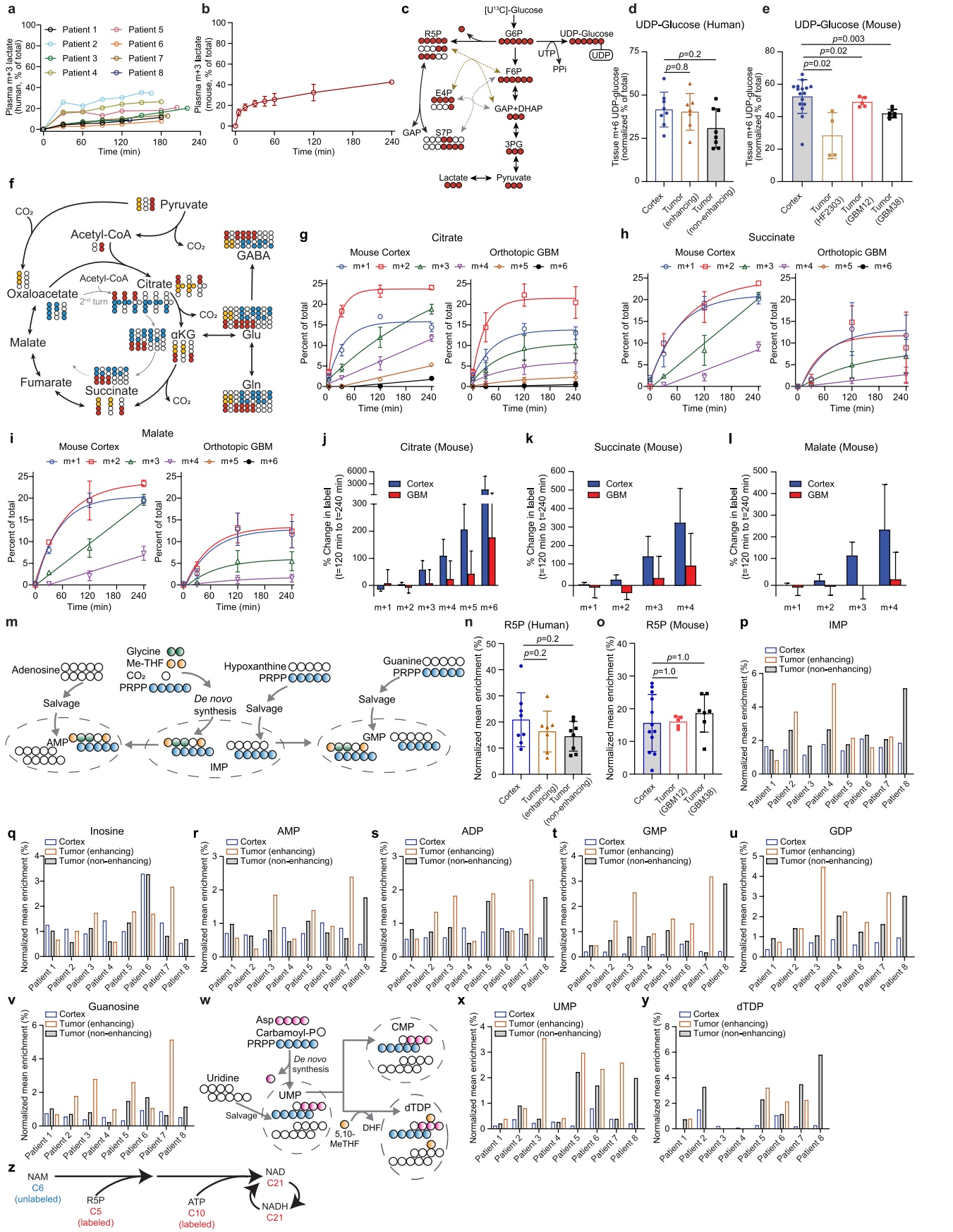

Extended Data Fig. 3 | See next page for caption.

Extended Data Fig. 3 | Glucose-derived labelling of tissue and plasma metabolites in patients and mice with brain tumours. a, Time course of m + 3 lactate in plasma from 8 patients infused with [U^{13}C]glucose. Plasma from patient 8 could not be analysed at time 0. **b**, Time course of m + 3 lactate in plasma from orthotopic GBM38 bearing mice (3–10 per timepoint) infused with [U^{13}C]glucose. Data are mean ± s.d. at each timepoint. **c**, Schema of glucose carbon (red circles) redistribution into glycolytic intermediates. Scrambling can occur via recombination with unlabelled intermediates in the pentose phosphate cycle (E4P, S7P, R5P, GAP). **d**, Normalized enrichment of m + 6 UDP-glucose in intracranial tissues from 8 glioma patients infused with [U^{13}C]glucose. **e**, Normalized enrichment of m + 6 UDP-glucose enrichment in cortex and orthotopic GBM tissue isolated from intracranial tumour-bearing mice infused with [U^{13}C]glucose. **f**, Schema of ^{13}C-labelling in TCA cycle intermediates and neurotransmitters arising from m + 3 pyruvate. Red circles indicate entry through pyruvate dehydrogenase, and gold circles indicate entry through pyruvate carboxylase. Blue circles indicate labelling patterns possible on second TCA cycle turn. **g-i**, Isotopologue abundance levels of citrate (**g**), succinate (**h**), and malate (**i**) in cortex and GBM tissues at indicated time points from orthotopic GBM38-bearing mice infused with [U^{13}C]glucose. **j-l**, Percent change in citrate (**j**), succinate (**k**), and malate (**l**) isotopologues from 120 to 240 min in mice infused with [U^{13}C]-glucose. **m**, Schema of purine synthetic pathways. Green and yellow circles indicate glycine- and folate-derived carbons, respectively. Blue circles indicate R5P-derived carbons. Partial shading of these circles indicates that a variety of labelling patterns are possible. **n**, Normalized enrichment of R5P in intracranial tissues from 8 glioma patients infused with [U^{13}C]glucose. **o**, Normalized enrichment of R5P in cortex and orthotopic GBM tissue isolated from intracranial tumour-bearing mice infused with [U^{13}C]glucose. **p-v**, Normalized enrichment of IMP (**p**), inosine (**q**), AMP (**r**), ADP (**s**), GMP (**t**), GDP (**u**), and guanosine (**v**) in intracranial tissues from glioma patients infused with [U^{13}C]glucose. **w**, Schema of pyrimidine synthetic pathways. Magenta indicates aspartate-derived carbons, blue indicates R5P-derived carbons, and yellow indicates folate-derived carbons. Partial shading is used to indicate that a variety of labelling patterns are possible. **x**,**y**, Normalized enrichment of UMP (**x**) and dTDP (**y**) in intracranial tissues from glioma patients infused with [U^{13}C]glucose. **z**, Schematic of carbon incorporation into NAD and NADH. In **d**, **e**, **n**, and **o**, data are mean ± s.d. of metabolite enrichments normalized to labelled plasma glucose on a per-patient or per-mouse basis. Comparisons between groups were performed using linear mixed-effects models with a random intercept for individual, and multiple pairwise comparisons across tissue types were adjusted using Holm's method. All statistical tests were two-sided. For mice, n = 4–16 samples per group were from 16 mice (4–7 mice for each orthotopic model with cortex samples from all mice pooled) were analysed. For humans, n = 7–8 samples per group were analysed. Some metabolites were not reliably detected in every tissue sample and were therefore not shown. In **g**, **h**, and **i**, data are mean ± s.d. of n = 3–9 samples from 1–3 mice per timepoint. In **j**, **k**, and **l**, data are mean ± s.d. Error bars are propagated from uncertainty in t = 120 and t = 240 min datapoints. n = 9 samples from 3 mice per time point. In **c**, **f**, **m**, **w**, and **z**, some intermediates are omitted from pathway diagrams for conciseness. Abbreviations: G6P (glucose 6-phosphate), F6P (fructose 6-phosphate), DHAP (dihydroxyacetone phosphate), GAP (glyceraldehyde 3-phosphate), 3PG (3-phosphoglycerate), R5P (ribose 5-phosphate), E4P (erythrose 4-phosphate), S7P (sedoheptulose 7-phosphate), PRPP (phosphoribosyl pyrophosphate), Me-THF (N10-formyltetrahydrofolate), 5,10-MeTHF (5,10-methylenetetrahydrofolate), NAM (nicotinamide).

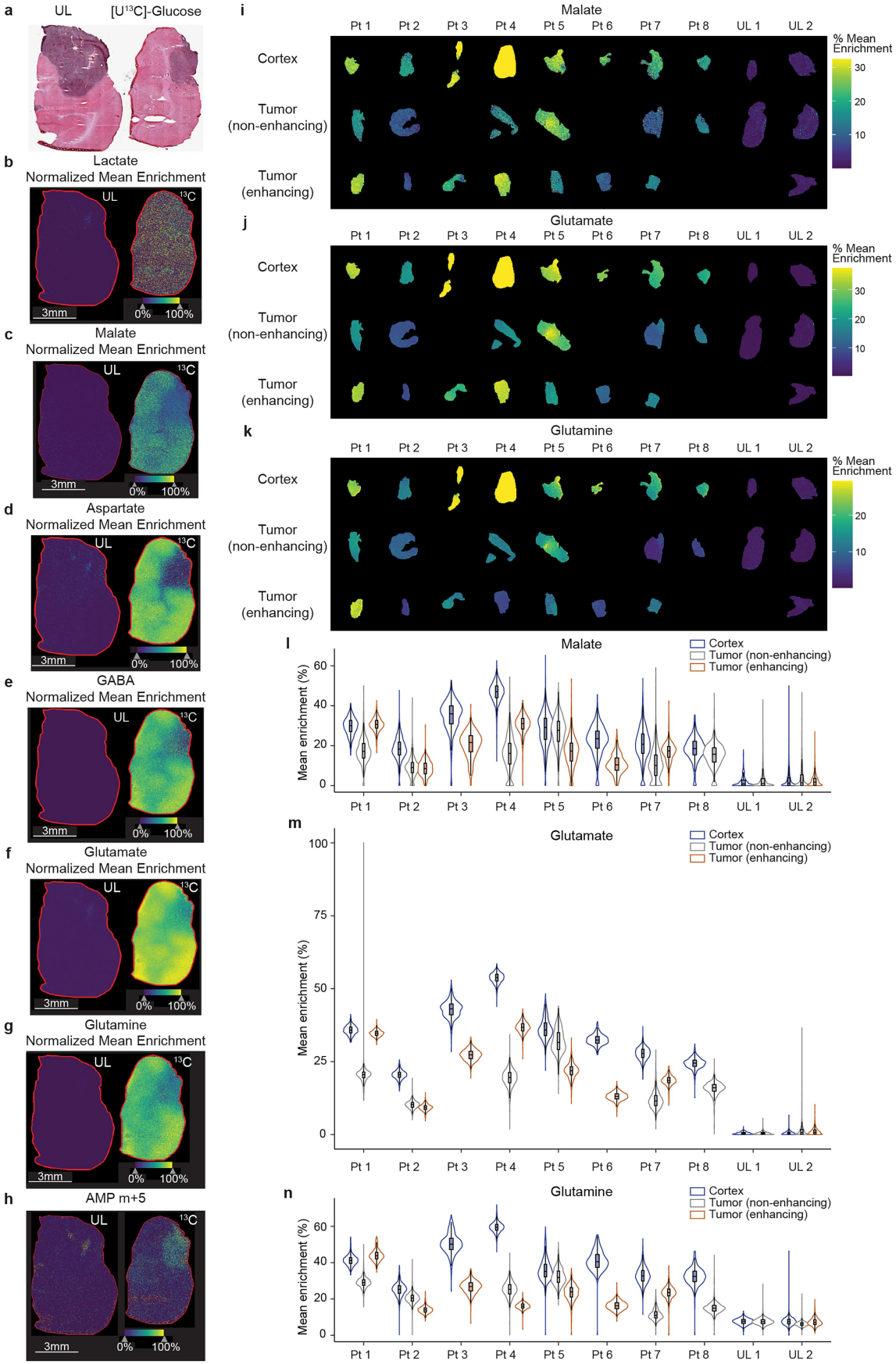

Extended Data Fig. 4 | See next page for caption.

Extended Data Fig. 4 | Spatially defined isotope labelling in cortex and GBM. a, H&E staining of brains from orthotopic GBM bearing mice intraperitoneally injected with either vehicle (left) as a negative control or [U^{13}C]glucose (right). **b-h**, MALDI-MS was used to determine ^{13}C enrichment of lactate (**b**), malate (**c**), aspartate (**d**), GABA (**e**), glutamate (**f**), glutamine (**g**), and AMP m + 5 (**h**). Tissue maximum is set to 100%. **i-k**, Tissues resected from brain cancer patients receiving either [U^{13}C]glucose infusion (patients 1–8) or no infusion (UL 1–2) were assessed by MALDI-MS for ^{13}C isotope labelling of malate (**i**), glutamate (**j**), and glutamine (**k**). Colour bar maximum set at true enrichment. **l-n**, Quantification of ^{13}C-labelling of malate (**l**), glutamate (**m**), and glutamine (**n**) for all data points (pixel values) from spatial MALDI-MS scans shown in panels i-k and Fig. 2e. In box plots, centre line represents median, box limits represent upper and lower quartiles, and whiskers show 1.5x interquartile range. Outlier points are hidden. Violin plots are trimmed to the range of the data. All violins have the same maximum width. For **a** and **b**, the images of ^{13}C-labelled tissues are also shown in Fig. 1g. For **c**, the image of ^{13}C-labelled tissue is also shown in Fig. 2f. For **h**, the image of ^{13}C-labelled tissue is also shown in Fig. 2i. For **i**, the images corresponding to patient 7 are also shown in Fig. 2e. Abbreviations: UL (unlabelled).

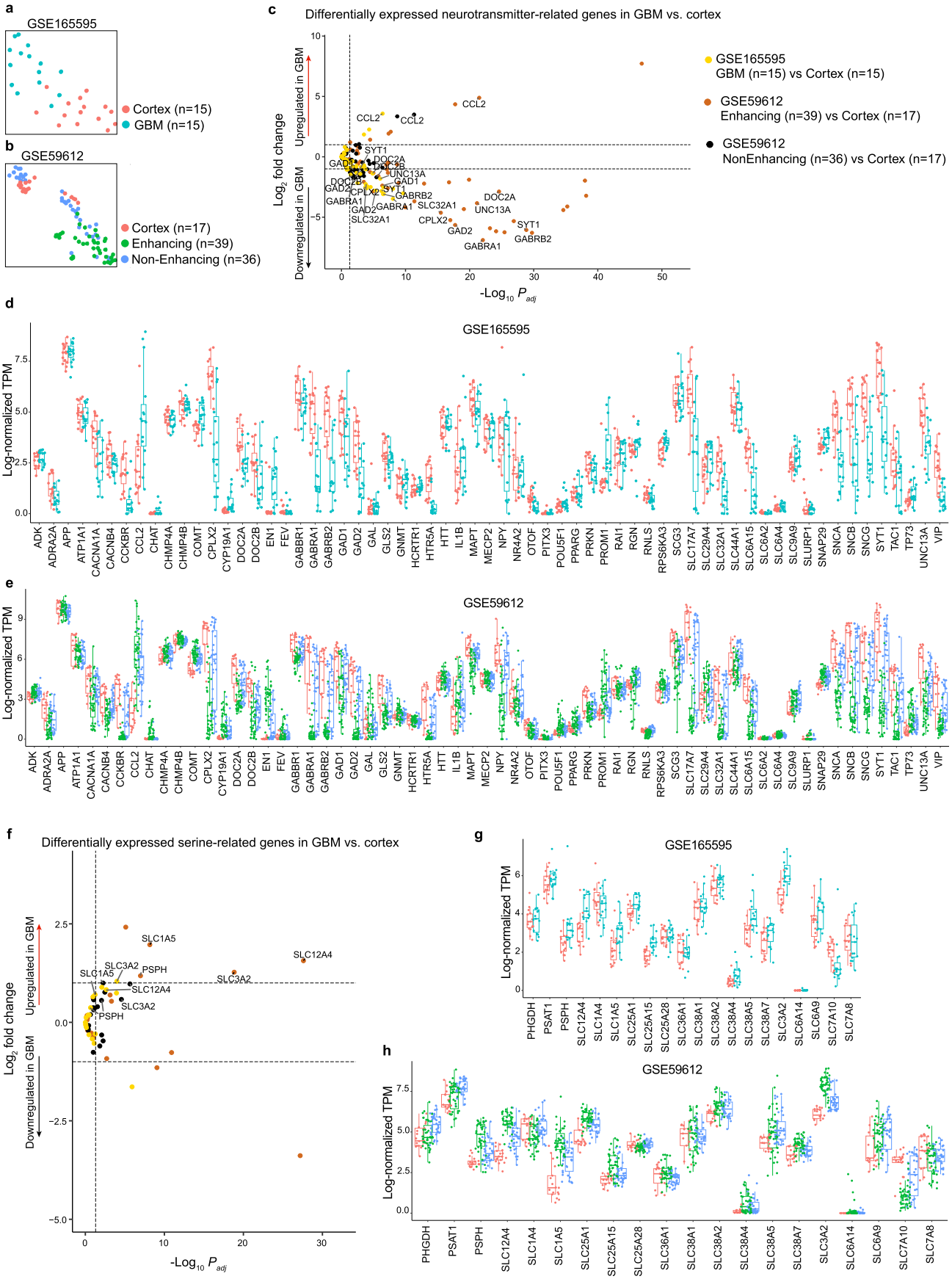

Extended Data Fig. 5 | See next page for caption.

Extended Data Fig. 5 | Transcriptional analysis of neurotransmitter signalling and serine metabolism genes in GBM and cortex. a,**b**, UMAP visualization based on expression of all genes in the GSE165595 RNA-seq dataset[64] (**a**) for cortex and GBM tissues and GSE59612 RNA-seq dataset[65] (**b**) for cortex, enhancing, and non-enhancing tissues. Number of nearest neighbours in UMAP is 13 for (**a**) and 15 for (**b**). n represents number of samples for each group. **c**, Volcano plot of differentially expressed neurotransmitter genes in tumour compared to the cortex in both datasets. **d**,**e**, Transcriptional expression of neurotransmitter-related genes in GSE165595 (**d**) and GSE59612 (**e**). **f**, Volcano plot of differentially expressed serine synthesis and serine transporter genes in tumour compared to the cortex in both datasets. **g**,**h**, Transcriptional expression of serine-related genes in GSE165595 (**g**) and GSE59612 (**h**). In (**c**) and (**f**), Log2 fold change represents the ratio of mean expression of a gene in tumour over cortex. Positive Log2 fold change indicates higher expression in tumour. P-values were adjusted using Benjamini-Hochberg test with the false discovery rate <0.05 and log2 fold change threshold was set to 1. In **d**-**e** and **g**-**h**, expression values are shown in log2(1+transcript per million) unit. Abbreviations: UMAP (Uniform Manifold Approximation and Projection).

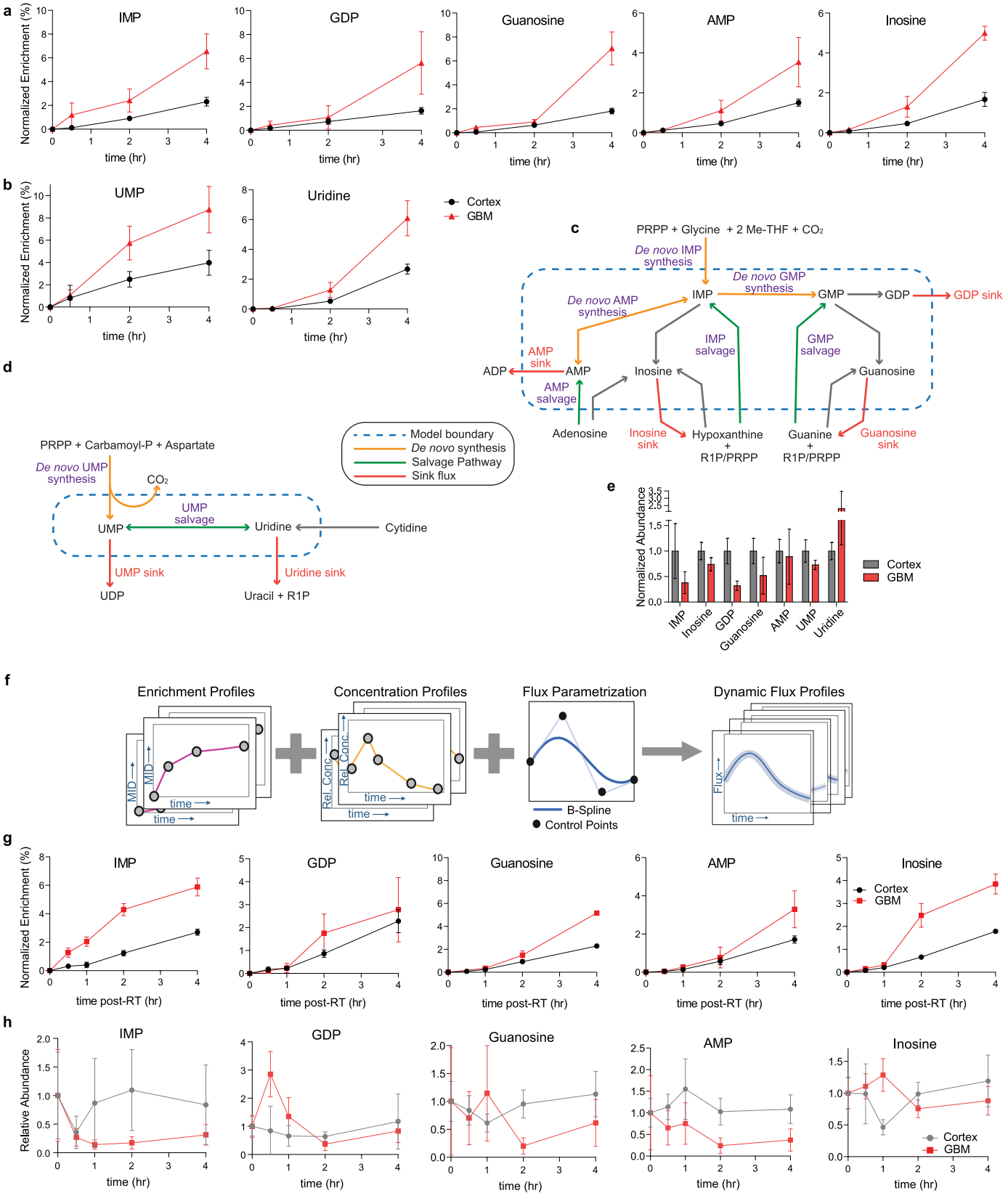

Extended Data Fig. 6 | See next page for caption.

Extended Data Fig. 6 | Dynamic incorporation of glucose carbons into nucleotide metabolites and in vivo modelling frameworks. a, Time-dependent enrichment profiles of purine metabolites IMP, GDP, guanosine, AMP, and inosine in orthotopic GBM38-bearing mice infused with [$U^{13}C$]glucose. Data are mean ± s.d. of n = 3–9 samples from 1–3 mice per timepoint. **b**, Time-dependent enrichment of pyrimidine metabolites UMP and uridine in orthotopic GBM38-bearing mice infused with [$U^{13}C$]glucose. Data are mean ± s.d. of n = 3–9 samples from 1–3 mice per timepoint. **c-d**, Biochemical interconversions and model boundaries used for metabolic modelling of purine synthesis (**c**) and pyrimidine synthesis (**d**). **e**, Relative abundance of nucleotide species in cortical and GBM tissues from orthotopic tumour bearing mice. **f**, Schema of dynamic metabolic flux analysis pipeline. The diagram was created using BioRender. **g-h**, Isotope enrichment (**g**) and relative abundance (**h**) of purine metabolites IMP, GDP, guanosine, AMP, and inosine in tissues from orthotopic GBM38-bearing mice treated with a single dose of cranial RT (8 Gy) and then immediately infused with [$U^{13}C$]glucose. Data are mean ± s.d. of n = 3–9 samples from 1–3 mice per timepoint. For **a**, **b**, and **g**, time-course enrichment data normalization to plasma glucose is detailed at https://github.com/baharm1/iMFA/. Abbreviations: PRPP (phosphoribosyl pyrophosphate), R1P (ribose 1-phosphate), Me-THF (10-formyltetrahydrofolate).

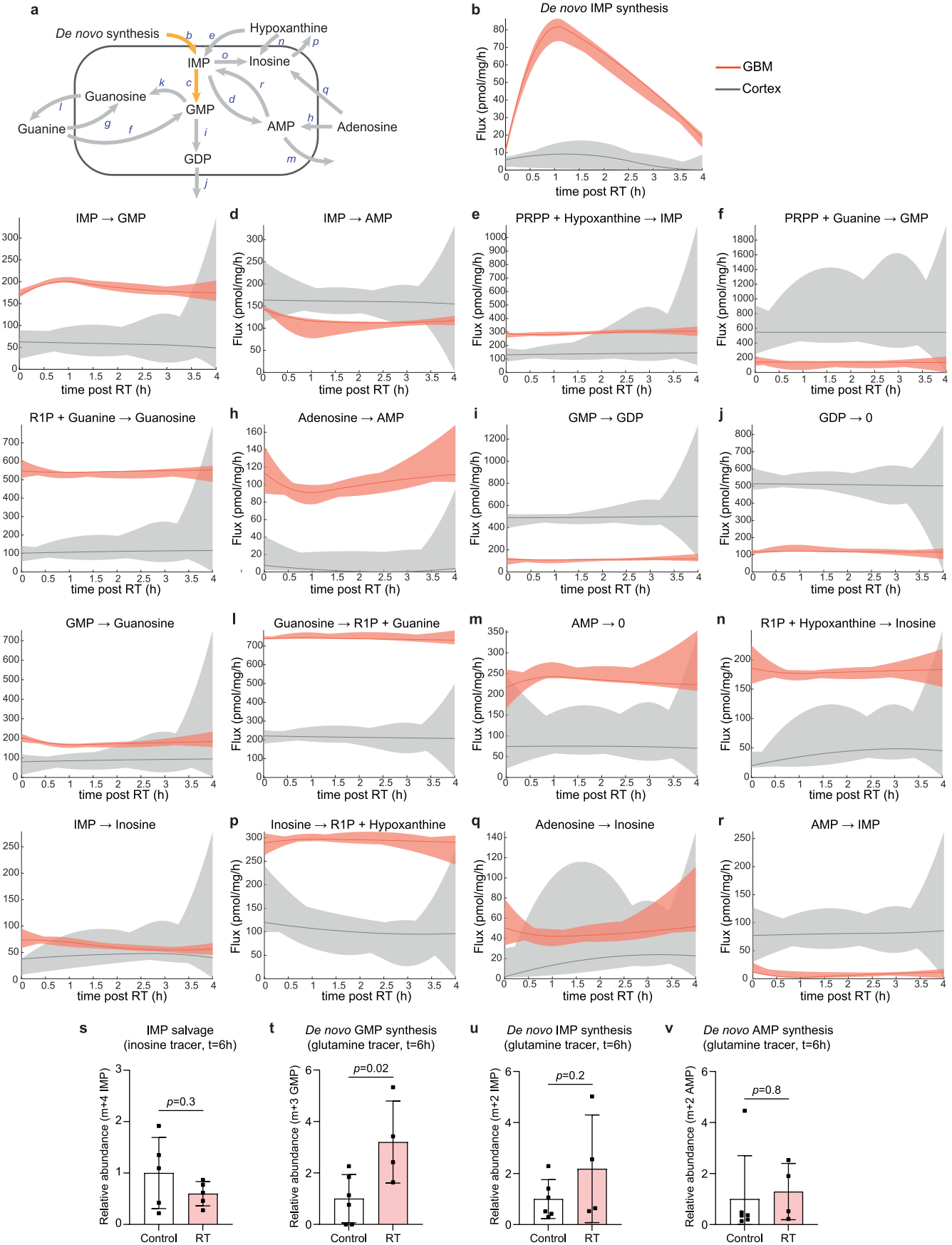

Extended Data Fig. 7 | See next page for caption.

Extended Data Fig. 7 | Dynamic metabolic response to radiation therapy in GBM and cortex. a, Fluxes through purine synthesis after RT estimated by analysing orthotopic tumour and cortex tissues from GBM38-bearing mice that were treated with whole cranial RT (8 Gy), immediately (<5 min post-RT) infused with [U^{13}C]glucose and serially euthanized at varying timepoints following treatment. **b**-**r**, Flux values for the following reactions were approximated using time-course enrichment as described in Supplementary Methods: de novo IMP synthesis (**b**), conversion of IMP to GMP (**c**), conversion of IMP to AMP (**d**), conversion of PRPP + hypoxanthine to IMP (**e**), conversion of PRPP + guanine to GMP (**f**), conversion of R1P + guanine to guanosine (**g**), conversion of adenosine to AMP (**h**), conversion of GMP to GDP (**i**), GDP exit from model boundary (**j**), conversion of GMP to guanosine (**k**), conversion of guanosine + R1P to guanine (**l**), AMP exit from model boundary (**m**), conversion of R1P + hypoxanthine to inosine (**n**), conversion of IMP to inosine (**o**), conversion of inosine to R1P + hypoxanthine (**p**), conversion of adenosine to inosine (**q**), and conversion of AMP to IMP (**r**). Solid lines indicate estimated fluxes, and shaded regions indicate 95% confidence intervals. Fluxes were approximated using 3–9 samples per timepoint with samples originating from 1–3 mice per group and 3 samples per mouse. **s**, Levels of m + 4 IMP in orthotopic GBM38 tumours harvested from control or cranial RT (8 Gy)-treated mice infused with $^{15}N_4$-inosine. Data are mean ± s.d. of tumour samples from 4–5 mice per group containing 1–2 tumour foci each. **t**-**v**, Relative levels of de novo m + 3 GMP (**t**), de novo m + 2 IMP or (**u**) de novo m + 2 AMP (**v**) in orthotopic GBM38 tumours harvested from control or cranial RT (8 Gy)-treated mice infused with ^{15}N-glutamine. Data are mean ± s.d. of tumour samples isolated from 3 mice per group containing 1–3 intracranial tumour foci each. In **s**-**v**, groups were compared by t-test. Abbreviations: PRPP (phosphoribosyl pyrophosphate), R1P (ribose 1-phosphate).

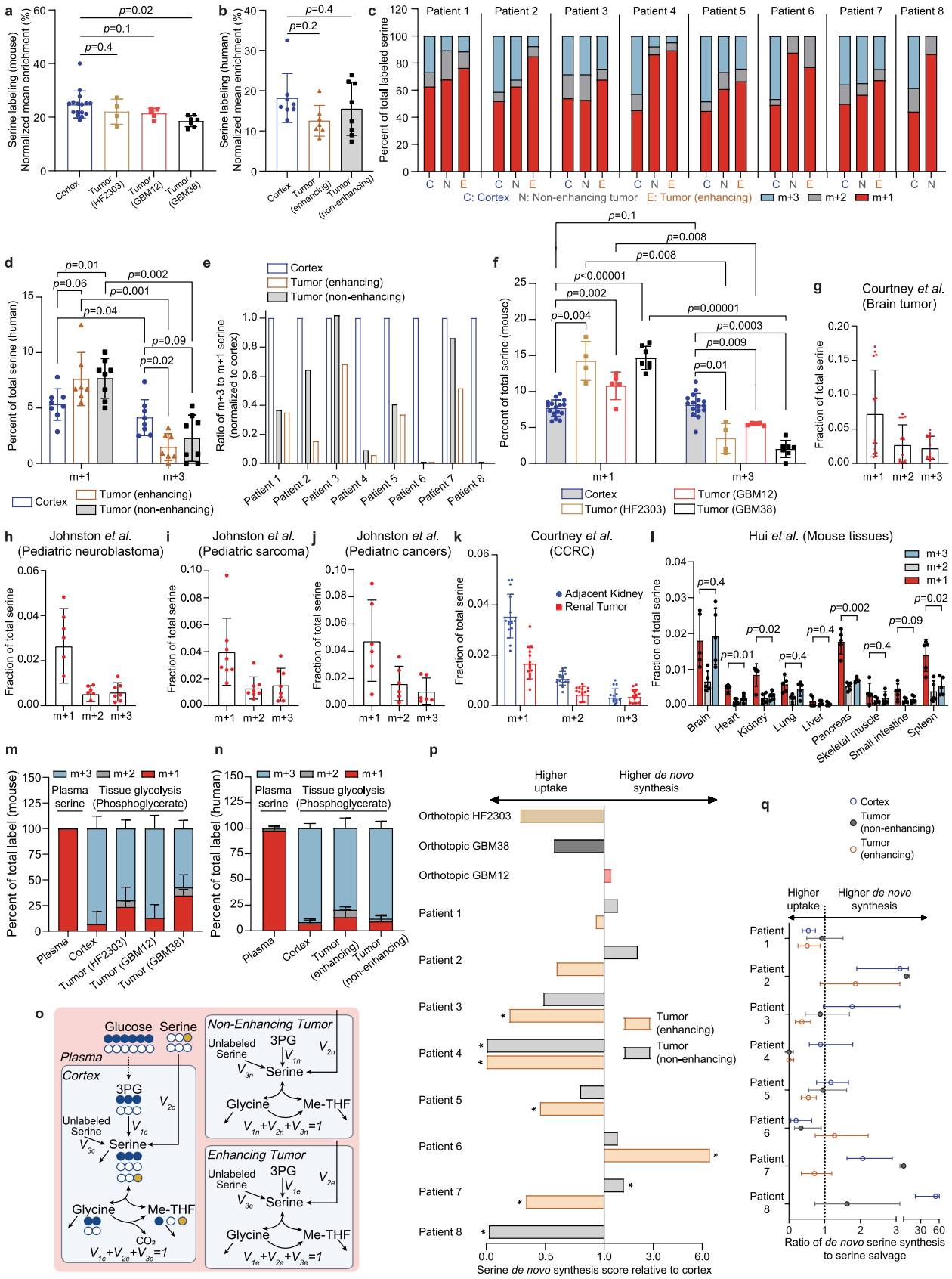

Extended Data Fig. 8 | See next page for caption.

Extended Data Fig. 8 | Rewiring of glucose-derived serine synthesis and its environmental uptake in tumours. a, Normalized (to labelled plasma glucose on a per-mouse basis) enrichment of serine in cortex and orthotopic GBM tissue isolated from intracranial tumour-bearing mice infused with [U^{13}C]glucose. **b**, Normalized (to labelled plasma glucose on a per-patient basis) enrichment of serine in intracranial tissues from 8 glioma patients infused with [U^{13}C]glucose. **c**, Serine isotopologue distributions (normalized to total serine labelling) in intracranial tissues from 8 human brain cancer patients infused with [U^{13}C]glucose. **d**, Percent of serine that contains one (m + 1) or three (m + 3) tracer-derived ^{13}C atoms in intracranial tissues from 8 glioma patients infused with [U^{13}C]glucose. **e**, Ratios of m + 3 serine to m + 1 serine in intracranial tissues from 8 human brain cancer patients infused with [U^{13}C]glucose. **f**, Percent of serine that contains one (m + 1) or three (m + 3) tracer-derived ^{13}C atoms in cortex and orthotopic GBM tissue isolated from intracranial tumour-bearing mice infused with [U^{13}C]glucose. **g**, Isotopic enrichment of serine in brain tumours from patients infused with [U^{13}C]glucose were plotted from supplementary data reported by Courtney et al.[11] **h-j**, Isotopic enrichment of serine in different paediatric tumour types including paediatric neuroblastoma (**h**), paediatric sarcoma (**i**), and a variety of other miscellaneous paediatric cancers (**j**) was previously reported as supplementary information by Johnston et al.[43] and re-plotted here. **k**, The work of Courtney et al. includes supplementary information reporting enrichment of serine in clear cell renal cell carcinoma (CCRC) and adjacent kidney tissue. **l**, The work of Hui et al.[26] includes ^{13}C serine labelling information in multiple tissue types from mice infused with [U^{13}C]glucose. **m**, Isotopologue distributions of plasma serine and tissue phosphoglycerate in cortex and orthotopic GBM tissue isolated from intracranial tumour-bearing mice infused with [U^{13}C]glucose. **n**, Isotopologue distributions of plasma serine and tissue phosphoglycerate in intracranial tissues from 8 glioma patients infused with [U^{13}C]glucose. **o**, Metabolic flux analysis model used to estimate scores of de novo serine synthesis to serine uptake ratios in brain cancer patients and orthotopic GBM-bearing mice infused with [U^{13}C]glucose. The model was used to quantify serine acquisition routes in cortex and gliomas. **p**, Relative (to cortex) reliance on serine uptake compared to glucose-driven de novo serine synthesis in mice and humans infused with [U^{13}C]glucose. Significance levels of tumour vs. adjacent cortex were tested by comparing 95% confidence intervals with $p < 0.05$ (indicated by asterisk) defined by non-overlapping groups. **q**, Ratio of contribution of de novo serine synthesis to serine uptake in human cortex and brain cancers. Error bars represent 95% confidence intervals. In **a**, **b**, **d**, **f**, **m**, and **n**, data are mean ± s.d. In **a**, **b**, **d**, and **f**, comparisons between groups were performed using linear mixed effects models with Holm's correction. In **a** and **f**, n = 4–16 samples per group from 16 mice (4–7 mice for each orthotopic model with cortex samples from all mice pooled). In **b** and **d**, n = 7–8 samples per group. In **g-l**, data are mean ± s.d. Comparisons between groups were performed using linear mixed effects models.

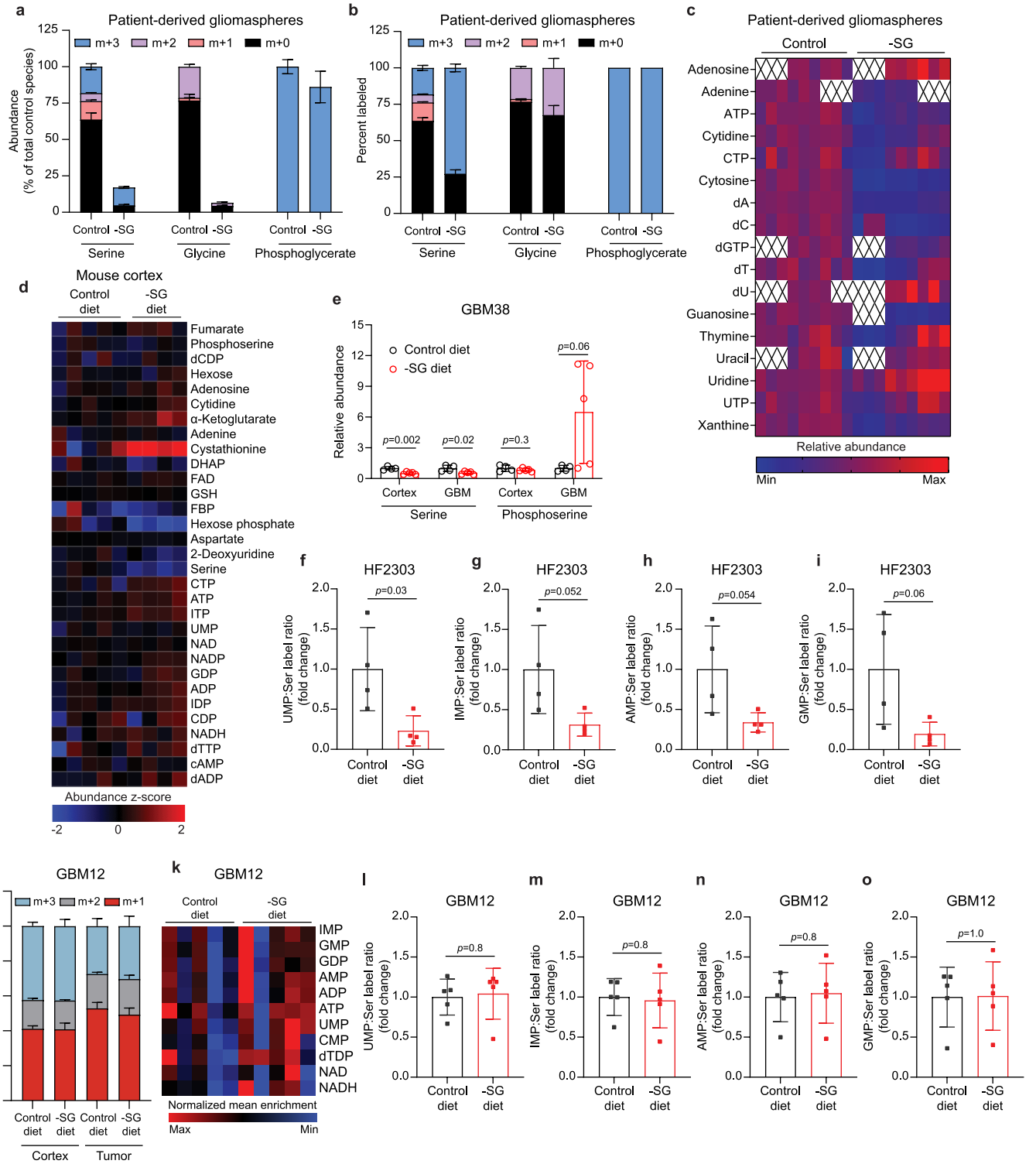

Extended Data Fig. 9 | See next page for caption.

Extended Data Fig. 9 | Differential metabolic effects of exogenous serine restriction on patient-derived GBM models and mouse cortex. **a**, Abundance of serine, glycine, and phosphoglycerate in 374gs gliomaspheres labelled with [U^{13}C]glucose in control media or media without serine and glycine. **b**, Mass isotopologue distributions of serine, glycine, and phosphoglycerate in 374gs gliomaspheres labelled with [U^{13}C]glucose in control media or media without serine and glycine. In **a** and **b**, data are mean ± s.e.m. n = 9 samples per group from 3 independent experiments each with 3 samples per condition. **c**, Heatmap of relative nucleotide abundance in 374gs gliomaspheres under control or environmental serine/glycine-depleted conditions. Each column represents one of 9 biological replicates from 3 independent experiments each with 3 samples per condition. A white box containing an X indicates not detected in this replicate. **d**, Metabolite levels in cortical tissue from intracranial GBM38-bearing mice on a control or serine/glycine-restricted diet. **e**, Relative serine and phosphoserine levels in GBM38 tumours and cortex from mice fed control or Ser/Gly-restricted diets. Data are mean ± s.d. Comparisons between groups were performed by t-test. n = 4–5 mice per group. **f**, UMP:Ser label ratios in HF2303 tumours from mice on control or -SG diets. **g**, IMP:Ser label ratios in HF2303 tumours from mice on control or -SG diets. **h**, AMP:Ser label ratios in HF2303 tumours from mice on control or -SG diets. **i**, GMP:Ser ratios in HF2303 tumours from mice on control or -SG diets. **f-i**, Label ratios are defined as ratio (relative to control) of ^{13}C-glucose-derived nucleotide enrichments (% labelled carbons) to glycolysis-derived m + 3 serine (% of total serine) in HF2303 tumours from mice infused with [U^{13}C]glucose. Data are mean ± s.d. Data were generated from 3–4 mice per group with 1–2 tumour foci per mouse. Comparisons between groups were performed by two-sided t-test. **j**, Isotopologue distributions of labelled serine in intracranial GBM12 tumour-bearing mice infused with [U^{13}C]glucose. **k**, Heatmap showing normalized (to labelled plasma glucose on a per-mouse basis) enrichment of biosynthesis intermediates in GBM12 tumours from intracranial GBM-bearing mice infused with [U^{13}C]glucose. **l**, UMP:Ser ratios in GBM12 tumours from mice on control or -SG diets. **m**, IMP:Ser ratios in GBM12 tumours from mice on control or -SG diets. **n**, AMP:Ser ratios in GBM12 tumours from mice on control or -SG diets. **o**, GMP:Ser ratios in GBM12 tumours from mice on control or -SG diets. **l-o**, Label ratios are defined as ratio (relative to control) of ^{13}C-glucose-derived nucleotide enrichments (% labelled carbons) to glycolysis-derived m + 3 serine (% of total serine) in GBM12 tumours from mice infused with [U^{13}C]glucose. Data are mean ± s.d. Data were generated from 5 mice per group. Comparisons between groups were performed by two-sided t-test.

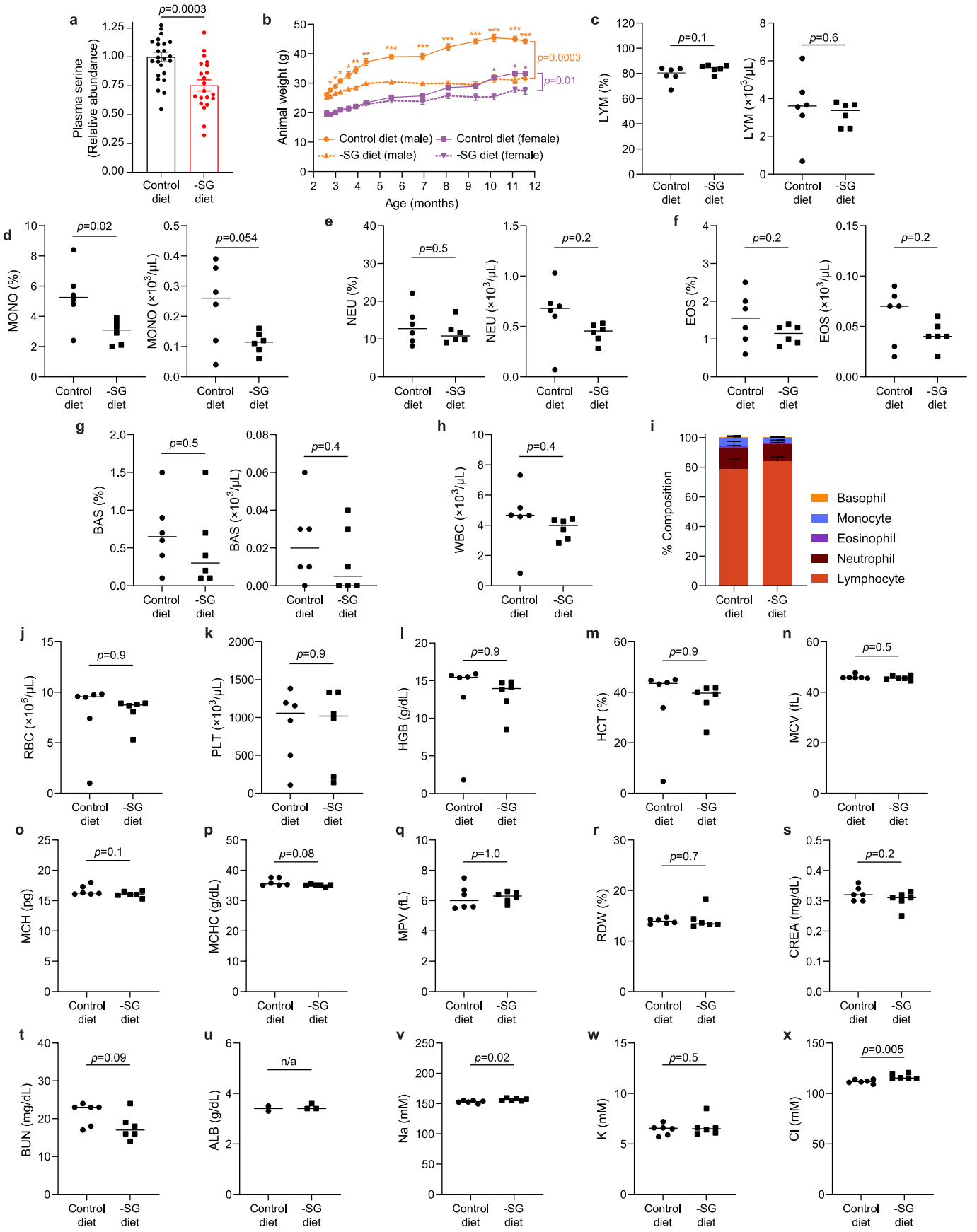

Extended Data Fig. 10 | See next page for caption.

Extended Data Fig. 10 | Biochemical and physiological effects of dietary serine/glycine restriction in mice. a, Abundance of serine in plasma from intracranial GBM-bearing mice fed either control diets or serine/glycine-restricted diets for 4 weeks. Data are mean ± s.e.m., and groups were compared by t-test. n = 21–25 mice bearing intracranial HF2303, GBM38 or GBM12 tumours per group from 5 independent experiments. **b**, Weights of mice fed control diets or serine/glycine-restricted diets. Data are mean ± s.e.m., and differences between control diet groups and serine/glycine-restricted diet groups for each sex were compared by t-test with Holm-Šídák correction. n = 5 mice per group. *$p \leq 0.05$; **$p \leq 0.01$, ***$p \leq 0.001$. **c-x**, Complete blood counts (**c-r**) and serum chemistries (**s-x**) were analysed for C57BL/6 J mice fed either a control diet or serine/glycine-restricted diet for 9 months. **c**, Lymphocyte percentage of white blood cells and lymphocyte counts. **d**, Monocyte percentage of white blood cells and monocyte counts. **e**, Neutrophil percentage of white blood cells and neutrophil counts. **f**, Eosinophil percentage of white blood cells and eosinophil counts. **g**, Basophil percentage of white blood cells and basophil counts. **h**, White blood cell counts. **i**, White blood cell distributions. Data are mean ± s.d. **j**, Red blood cell counts. **k**, Platelet counts. **l**, Haemoglobin concentrations. **m**, Haematocrit. **n**, Mean corpuscular volume. **o**, Mean corpuscular haemoglobin. **p**, Mean corpuscular haemoglobin concentration. **q**, Mean platelet volume. **r**, Red blood cell distribution width. **s**, Creatinine. **t**, Blood urea nitrogen. **u**, Albumin. **v**, Sodium. **w**, Potassium. **x**, Chloride. **c-x**, Lines represent means. Groups were compared by t-test with n = 6 mice per group except for albumin measurements in panel **u** (n = 2–3 mice per group), in which experimentation was limited by sample volume and no statistical comparison could be made. Abbreviations: LYM (lymphocyte), MONO (monocyte), NEU (neutrophil), EOS (eosinophil), BAS (basophil), WBC (white blood cell), RBC (red blood cell), PLT (platelet), HGB (haemoglobin), HCT (haematocrit), MCV (mean corpuscular volume), MCH (mean corpuscular haemoglobin), MCHC (mean corpuscular haemoglobin concentration), MPV (mean platelet volume), RDW (RBC distribution width), CREA (creatinine), BUN (blood urea nitrogen), ALB (albumin), Na (sodium), K (potassium), Cl (chloride).

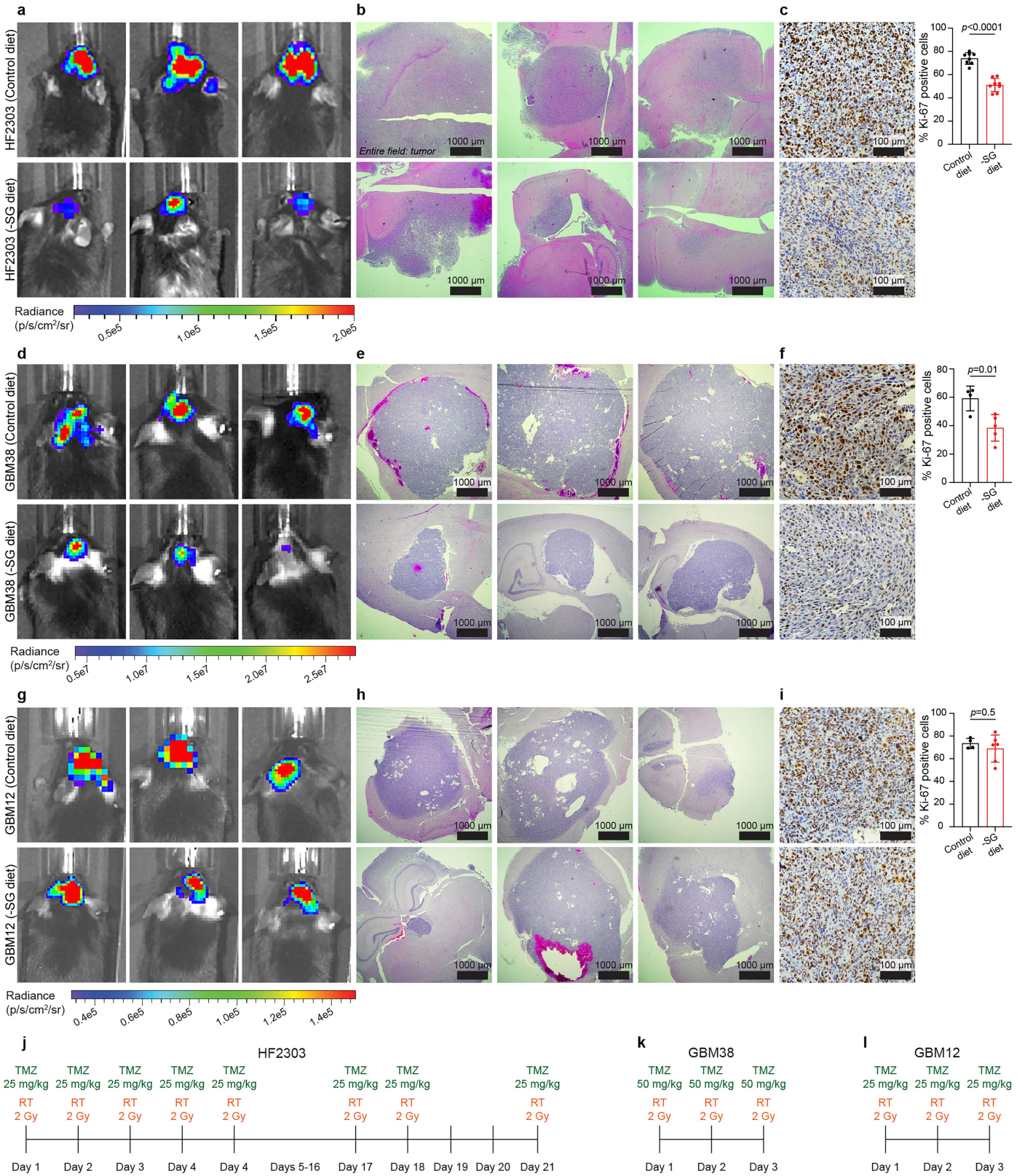

Extended Data Fig. 11 | See next page for caption.

Extended Data Fig. 11 | Effects of dietary serine/glycine restriction on intracranial tumour burden in GBM-bearing mice. a, Representative bioluminescence imaging of luciferase-positive HF2303 tumours grown orthotopically in mice on control or -SG diets. **b**, Representative H&E staining of HF2303 tumour-containing brain tissue from mice on control or -SG diets. One control image shows only tumour tissue (top left, uniform dark purple staining) due to tumour size exceeding field. **c**, Representative Ki-67 immunohistochemistry of intracranial HF2303 tumour tissue from mice on control or -SG diets and quantification of Ki-67 positivity. Quantitative data are mean ± s.d. with n = 8 mice per group. Comparisons between groups were performed by t-test. **d**, Representative bioluminescence imaging of luciferase-positive GBM38 tumours grown orthotopically in mice on control or serine/glycine-restricted diets. **e**, Representative H&E staining of GBM38 tumour-containing brain tissue from mice on control or -SG diets. **f**, Representative Ki-67 immunohistochemistry of intracranial GBM38 tumour tissue from mice on control or -SG diets and quantification of Ki-67 positivity. Quantitative data are mean ± s.d. with n = 4–5 mice per group. Comparisons between groups were performed by t-test. **g**, Representative bioluminescence imaging of luciferase-positive GBM12 tumours grown orthotopically in mice on control or serine/glycine-restricted diets. **h**, Representative H&E staining of GBM12 tumour-containing brain tissue from mice on control or -SG diets. **i**, Representative Ki-67 immunohistochemistry of intracranial GBM12 tumour tissue from mice on control or -SG diets and quantification of Ki-67 positivity. Quantitative data are mean ± s.d. with n = 4–6 mice per group. Comparisons between groups were performed by t-test. **j-l**, Chemoradiation treatment schemes for intracranial GBM-bearing mice on control or -SG diets used in therapeutic efficacy studies of Fig. 4i–k. Tumour models used were HF2303 (**j**), GBM38 (**k**), and GBM12 (**l**).

Extended Data Table 1 | Clinical and molecular characteristics of patients studied with stable isotope tracing

Patient ID	Sex	Diagnosis	1p/19q Codeletion	MGMT Promoter Methylation	Ki-67 Index
P1	M	GBM	N/A	Equivocal (PCR)	30-40%
P2	F	GBM	N/A	Negative	30-40%
P3	M	GBM	N/A	Negative	70%
P4	F	Oligodendroglioma, IDH mutant, 1p/19q codeleted, WHO Grade 3	Positive	Unknown	15%
P5	M	GBM	N/A	Equivocal (PCR)	20-30%
P6	M	Diffuse hemispheric glioma, IDH wild-type, WHO Grade 4	Negative	Positive	15-40%
P7	M	GBM	N/A	Negative	>20%
P8	M	GBM	Negative	Negative	15%

nature portfolio

Corresponding author(s): Daniel R. Wahl, Deepak Nagrath, Wajd N. Al-Holou, Costas A. Lyssiotis

Last updated by author(s): Jul 15, 2025

Reporting Summary

Nature Portfolio wishes to improve the reproducibility of the work that we publish. This form provides structure for consistency and transparency in reporting. For further information on Nature Portfolio policies, see our Editorial Policies and the Editorial Policy Checklist.

Statistics

For all statistical analyses, confirm that the following items are present in the figure legend, table legend, main text, or Methods section.

n/a	Confirmed
☐	☒ The exact sample size (*n*) for each experimental group/condition, given as a discrete number and unit of measurement
☐	☒ A statement on whether measurements were taken from distinct samples or whether the same sample was measured repeatedly
☐	☒ The statistical test(s) used AND whether they are one- or two-sided *Only common tests should be described solely by name; describe more complex techniques in the Methods section.*
☐	☒ A description of all covariates tested
☐	☒ A description of any assumptions or corrections, such as tests of normality and adjustment for multiple comparisons
☐	☒ A full description of the statistical parameters including central tendency (e.g. means) or other basic estimates (e.g. regression coefficient) AND variation (e.g. standard deviation) or associated estimates of uncertainty (e.g. confidence intervals)
☐	☒ For null hypothesis testing, the test statistic (e.g. *F*, *t*, *r*) with confidence intervals, effect sizes, degrees of freedom and *P* value noted *Give P values as exact values whenever suitable.*
☐	☒ For Bayesian analysis, information on the choice of priors and Markov chain Monte Carlo settings
☒	☐ For hierarchical and complex designs, identification of the appropriate level for tests and full reporting of outcomes
☒	☐ Estimates of effect sizes (e.g. Cohen's *d*, Pearson's *r*), indicating how they were calculated

Our web collection on statistics for biologists contains articles on many of the points above.

Software and code

Policy information about availability of computer code

Data collection	The following software were used in data collection: Agilent MassHunter Profinder (version 10.0); Agilent MassHunter Quantitative Analysis (version B.08.02); Agilent Masshunter Workstation Software LC/MS Data Acquisition for 6400 Series Triple Quadrupole MS (version B.08.02); Bruker Daltonics SciLS Lab 2023b with an in-house script utilizing the SCiLS REST API (version 6.2.114), written in R (version 4.2.2), using RStudio (2022.12.0 Build 353); Bruker Daltonics SCiLS Lab 2023a with an in-house R (version 4.1.1) pipeline using rMSIproc (verson 0.3.1) and enviPat (version 2.7).
Data analysis	The following data analysis software were used: GraphPad Prism (version 10) R (versions 4.4.2 and 4.2.2) MATLAB R2021b with Artelys Knitro toolbox (version 12.4) MetaboScape (2023 version) TASQ (2022 version) FastQC (version 0.12.1) samtools (version 1.13) htseq-count (version 2.0.9) biomaRt library (version 2.54.0) Seurat (version 4.2.0) AUCell (version 1.28.0) MetaboAnalyst (versions 5.0 and 6.0) Maven (version 8.1.27.11) QuPath (version 0.5.1)

GenePattern ssGSEA (version 5)
GE02R (no version information found, accessed on Dec 27, 2024)
GlioVis (version 0.20)
AccuCor (version 0.3.1)
For flux studies using LC-MS data, custom code was used and deposited on GitHub: https://github.com/baharm1/iMFA/

For manuscripts utilizing custom algorithms or software that are central to the research but not yet described in published literature, software must be made available to editors and reviewers. We strongly encourage code deposition in a community repository (e.g. GitHub). See the Nature Portfolio guidelines for submitting code & software for further information.

Data

Policy information about availability of data

All manuscripts must include a data availability statement. This statement should provide the following information, where applicable:

- Accession codes, unique identifiers, or web links for publicly available datasets
- A description of any restrictions on data availability
- For clinical datasets or third party data, please ensure that the statement adheres to our policy

RNA-seq data generated in this study are accessible through GEO Series accession number GSE299102 (https://www.ncbi.nlm.nih.gov/geo/query/acc.cgi?acc=GSE299102). The two RNA-seq datasets used in this study are available through GEO with accession numbers of GSE59612 (https://www.ncbi.nlm.nih.gov/geo/query/acc.cgi?acc=GSE59612) and GSE165595 (https://www.ncbi.nlm.nih.gov/geo/query/acc.cgi?acc=GSE165595). For molecular subtype classification based on RNA-seq data, TCGA-GBM dataset was accessed from GDC portal (https://portal.gdc.cancer.gov/; Dec 13, 2024). All other data supporting the findings of this study are available within the paper and its supplementary contents.

Research involving human participants, their data, or biological material

Policy information about studies with human participants or human data. See also policy information about sex, gender (identity/presentation), and sexual orientation and race, ethnicity and racism.

Reporting on sex and gender	Sexes of the 8 participants were determined using the "Legal Sex" data element in the medical record. The small number of patients (6 men and 2 women) prevents well-powered analysis by sex.
Reporting on race, ethnicity, or other socially relevant groupings	We did not consider socially constructed or socially relevant categorization variables due to the small number of patients.
Population characteristics	Covariate-relevant population characteristics (sex, diagnosis, IDH status, 1p/19q deletion, MGMT promoter methylation, Ki-67 index) are shown in Extended Data Table 1.
Recruitment	We recruited patients undergoing standard-of-care craniotomies for resection of newly diagnosed brain tumors at the University of Michigan. Our study was limited to brain tumor patients undergoing tumor resection that would yield enough excess tissue for metabolomic analysis, introducing potential self-selection bias toward larger tumors. Thus, our findings may not be applicable to patients whose presentation and tumor burden require diagnostic biopsy alone rather than larger tumor resection.
Ethics oversight	This study was approved by the Institutional Review Board of the University of Michigan.

Note that full information on the approval of the study protocol must also be provided in the manuscript.

Field-specific reporting

Please select the one below that is the best fit for your research. If you are not sure, read the appropriate sections before making your selection.

☒ Life sciences ☐ Behavioural & social sciences ☐ Ecological, evolutionary & environmental sciences

For a reference copy of the document with all sections, see nature.com/documents/nr-reporting-summary-flat.pdf

Life sciences study design

All studies must disclose on these points even when the disclosure is negative.

Sample size	Sample sizes for animal experiments were determined by preliminary studies and the level of observed effect. Sample size for humans was determined by maximal enrollment.
Data exclusions	Mice failing to form intracranial tumors post-orthotopic implantation (<5%) or dying 0-5 days after implantation (<5%) or jugular/carotid catheter placement (<10%), likely due to surgical complications, were excluded. In LC-MS experiments, metabolites below detection thresholds were excluded. One mouse was excluded due to an unrelated condition requiring its humane euthanasia. The tumor sample from one control HF2303-bearing mouse with isotopic glucose infusion was excluded due to diffuse growth inseparable from cortical tissue. In developing our hypothesis-generating metabolic flux models of nucleotide synthesis, the need for multiple timepoints constrained sample numbers at each timepoint, and exclusions were necessary to minimize variance within groups and ensure data robustness. Corresponding

exclusion criteria are described at https://gitfront.io/r/baham1/31F7SiKgPJAw/iMFA/, and model-based predictions were validated by multiple orthogonal tracers.

Replication

Replication was limited by complexity of patient infusion studies and restricted tissue quantities; data from 8 human infusions are reported. In mice, labeled glucose infusion showed consistent tumor vs. cortex metabolic labeling in 3 orthotopic models in this study (GBM38 [≥3 times], HF2303, GBM12), matching human tracing. Similar consistency was observed in ≥5 serial labeled glucose injection experiments across HF2303, GBM38, and 2 additional models not presented. Isotopic serine infusion uptake was consistent across 3 models in this study (HF2303, GBM38, GBM12) and 1 additional model not shown, with GBM38 uptake replicated via tracer injection (not presented). Studies with amide-labeled glutamine infusions showed consistent GBM vs. cortex label patterns in ≥3 independent experiments. In vitro gliomasphere experiments were performed 3 times. All attempts at replicating the experiments were successful.

Randomization

Patients were not allocated into groups. Animal allocation was performed to achieve similar starting median tumor luminescence across groups.

Blinding

Blinding was not possible due to the complexity of multi-step procedures: group allocation, animal treatments, animal monitoring, data collection, and analyses were performed independently by separate investigators, including technicians unaware of hypotheses and without stake in outcome, minimizing bias.

Reporting for specific materials, systems and methods

We require information from authors about some types of materials, experimental systems and methods used in many studies. Here, indicate whether each material, system or method listed is relevant to your study. If you are not sure if a list item applies to your research, read the appropriate section before selecting a response.

Materials & experimental systems

n/a	Involved in the study
☐	☒ Antibodies
☐	☒ Eukaryotic cell lines
☒	☐ Palaeontology and archaeology
☐	☒ Animals and other organisms
☒	☐ Clinical data
☒	☐ Dual use research of concern
☒	☐ Plants

Methods

n/a	Involved in the study
☒	☐ ChIP-seq
☒	☐ Flow cytometry
☒	☐ MRI-based neuroimaging

Antibodies

Antibodies used

Anti-Ki-67 antibody was purchased from BD Biosciences (catalog 550609). Secondary antibody was included in the Vectastain Elite ABC Kit (PK-6102).

Validation

The anti-Ki-67 antibody (BD Biosciences 550609) used for immunohistochemistry was validated based on manufacturer testing (https://www.bdbiosciences.com/en-us/products/reagents/flow-cytometry-reagents/research-reagents/single-color-antibodies-ruo/purified-mouse-anti-ki-67.550609?tab=product_details), our results, and its extensive use in peer-reviewed literature (cited over 700 times with at least 10 published images) such as Cell Death Dis 11,19(2020). In our experiments, presence of Ki-67 in tumor and not host brain further indicates specificity and agrees with in vivo tumor models and clinical practice.
This antibody was developed for the immunohistochemistry application. Applications below have been tested by the manufacturer.
Source: Mouse IgG1, κ
Species Reactivity: Human (QC Testing), Mouse (Tested in Development), Rat, Rhesus (Reported)
Application: Flow cytometry (Routinely Tested), Immunohistochemistry-frozen, Immunohistochemistry-formalin (antigen retrieval required) (Tested During Development)

Eukaryotic cell lines

Policy information about cell lines and Sex and Gender in Research

Cell line source(s)

GBM374gs gliomaspheres were generated from a male patient at UCLA (Los Angeles, CA) by the laboratory of Dr. Harley Kornblum. GBM12 PDX tissue (from a male patient) and GBM38 PDX tissue (from a female patient) were generated at Mayo Clinic (Rochester, MN) by the laboratory of Dr. Jann Sarkaria. The HF2303 model was generated from a male patient at Henry Ford Hospital (Detroit, MI) and was provided by Dr. Alnawaz Rehemtulla, Dr. Ana deCarvalho, and the Henry Ford Health System.

Authentication

The GBM374gs gliomasphere model was authenticated regularly via short tandem repeat (STR) fingerprinting using the GenePrint 10 system (Laragen). All formal experiments using GBM12, GBM38, and HF2303 patient-derived models were conducted in vivo with the exception of in vitro culturing for lentiviral GFP/luciferase transduction, and were not authenticated beyond primary isolation. In vivo passage and marker retention ensured identity of these orthotopic models.

Mycoplasma contamination

All models cultured in vitro were tested regularly for mycoplasma using the MycoAlert Mycoplasma Detection Kit (Lonza) and confirmed negative.

Commonly misidentified lines (See ICLAC register)	No commonly misidentified lines were used.

Animals and other research organisms

Policy information about studies involving animals; ARRIVE guidelines recommended for reporting animal research, and Sex and Gender in Research

Laboratory animals	Mice of age 4-12 weeks at experiment start, strains B6.129S7-Rag1tm1Mom (Jackson 002216 or bred in-house) and C57BL/6J (Jackson 000664), were used in this study.
Wild animals	This study did not involve wild animals.
Reporting on sex	Sex-based analyses could not be performed in humans due to low sample number and was therefore not extensively performed in mice. All studies were carried out with a mix of male and female mice, except for the time-course glucose tracing experiment that comprised only female mice and was validated using non-glucose tracers in both male and female mice.
Field-collected samples	This study did not involve samples collected from the field.
Ethics oversight	All animal studies were performed at the University of Michigan according to protocols approved by the University of Michigan Institutional Animal Care and Use Committee (IACUC).

Note that full information on the approval of the study protocol must also be provided in the manuscript.

Plants

Seed stocks	N/A
Novel plant genotypes	N/A
Authentication	N/A